frontiers | Frontiers in Earth Science

TYPE Original Research
PUBLISHED 02 May 2025
DOI 10.3389/feart.2025.1578301

Check for updates

OPEN ACCESS

EDITED BY
Long Li,
University of Alberta, Canada

REVIEWED BY
Zhiwei Wang,
Hebei GEO University, China
Yu Dong,
Jilin University, China

*CORRESPONDENCE
Mingxin Duan,
dmxpap2015@163.com
Jimin Huang,
huangjimin@mail.cgs.gov.cn

RECEIVED 17 February 2025
ACCEPTED 09 April 2025
PUBLISHED 02 May 2025

CITATION
Liu L, Duan M, Huang J, Song H, Lin X and Zhan Y (2025) Petrogenesis and tectonic implications of the Early Jurassic syenogranite in the northern section of Zhangguangcai Range, NE China: insights from geochronology, geochemistry, and Lu-Hf isotopes.
Front. Earth Sci. 13:1578301.
doi: 10.3389/feart.2025.1578301

COPYRIGHT
© 2025 Liu, Duan, Huang, Song, Lin and Zhan. This is an open-access article distributed under the terms of the Creative Commons Attribution License (CC BY). The use, distribution or reproduction in other forums is permitted, provided the original author(s) and the copyright owner(s) are credited and that the original publication in this journal is cited, in accordance with accepted academic practice. No use, distribution or reproduction is permitted which does not comply with these terms.

Petrogenesis and tectonic implications of the Early Jurassic syenogranite in the northern section of Zhangguangcai Range, NE China: insights from geochronology, geochemistry, and Lu-Hf isotopes

Liye Liu[1,2,3,4], Mingxin Duan[1,3]*, Jimin Huang[1,3]*, Haonan Song[1,3], Xiangpeng Lin[1,3] and Yong Zhan[1,3]

[1]Harbin Center for Integrated Natural Resources Survey, China Geological Survey, Harbin, China, [2]The Northeast Geological Science and Technology Innovation Center of the China Geological Survey, Shenyang, China, [3]Observation and Research Station of Earth Critical Zone in Black Soil, Ministry of Natural Resources, Harbin, China, [4]School of Earth Sciences and Resources, China University of Geosciences Beijing, Beijing, China

The Lesser Xing'an-Zhangguangcai Range tectonic belt in northeastern China is located along the eastern margin of the Central Asian Orogenic Belt and serves as the key to understanding the tectonic transition between the Paleo-Asian Ocean and Paleo-Pacific regimes during the Early Mesozoic. This study presented the zircon U-Pb geochronology, Hf isotope, and whole-rock geochemistry of Early Jurassic syenogranites from the northern Zhangguangcailing Range. The LA-ICP-MS zircon dating result indicates a crystallization age of 194 ± 2 Ma. Integrated with regional data, this study confirmed that the Early Mesozoic magmatism in the region was concentrated in the Early Jurassic (180–200 Ma). The granites displayed typical arc-related features, including (1) high SiO_2 (70.59–76.81 wt.%), alkali enrichment ($Na_2O + K_2O$ = 7.65–8.38 wt.%), low Mg and Fe contents, classifying them as the high-K calc-alkaline metaluminous to weakly peraluminous (A/CNK = 0.99–1.04); (2) strong LREE enrichment with weak Eu anomalies (δEu = 0.44–0.81) and HREE depletion ($(La/Yb)_N$ = 3.38–16.17); and (3) enrichment in LILEs (Rb, K) with the corresponding depletion in HFSEs (Nb, Ta, and Ti). Harker diagrams showed negative correlations between SiO_2 and MgO, TiO_2, CaO, TFeO, P_2O_5, and Eu, indicating fractional crystallization involving amphibole, ilmenite, apatite, and feldspar. The zircon εHf(t) values (+2.7 to +5.0) and the corresponding Meso-to Neoproterozoic crustal model ages (T_{DM2} = 915–1067 Ma) suggested that the magma originated from partial melting of the Meso-Neoproterozoic mafic lower crust at amphibolite facies. The geochemical and isotopic data collectively identified these rocks as I-type granite. In a regional tectonic context, their formation was interpreted to reflect an active continental margin environment driven by the westward subduction of the Paleo-Pacific Plate during the Early Jurassic, potentially influenced by the closure of the Mudanjiang Ocean, a branch of the Paleo-Pacific.

KEYWORDS

I-type granite, Zhangguangcai Range, lithogeochemistry, U-Pb age, Hf isotop-ic

1 Introduction

Northeast China has experienced extensive phanerozoic magmatism, producing large volumes of Paleozoic-Mesozoic granitoids (Wu et al., 2011; Xu et al., 2013b). Zircon geochronology demonstrates that regional magmatic activity mainly occurred from the Late Paleozoic to Early Mesozoic, with subordinate events occurring during the Neoproterozoic-Early Paleozoic (Ge et al., 2017; Ge et al., 2018). Mesozoic magmatism occurred in three distinct stages: Late Triassic-Early Jurassic (205–158 Ma), Late Jurassic-Early Cretaceous (157–136 Ma), and Late Cretaceous (135–90 Ma) (Ji et al., 2021; Yang et al., 2022). Late Triassic-Early Jurassic granitoids, including quartz diorite, granodiorite, monzogranite, and syenogranite with minor alkali feldspar granite, generally exhibit medium-to high-K calc-alkaline affinities (Xu et al., 2009; Xu M. J. et al., 2013; Li et al., 2016; Ge et al., 2017; Ge et al., 2018; Yin et al., 2021; Zhang et al., 2021). Geochemical trends have consistently shown decreasing P_2O_5 with increasing SiO_2 (Dong et al., 2017; Zhou et al., 2018; Duan et al., 2021), and these rocks are metaluminous to weakly peraluminous (A/CNK <1.1; Liu et al., 2017). Predominantly composed of I- and A-type granites with limited S-type occurrences (Ge et al., 2017; Ge et al., 2018), these plutons record the extended histories of fractional crystallization (Wu et al., 2003a; Wu et al., 2003b). The spatiotemporal distributions demonstrate a westward younging trend of Late Paleozoic-Mesozoic granitoids (Ge et al., 2020a; Ge et al., 2020b), and their Sr-Nd-Hf isotopic compositions reflect juvenile crustal sources, signifying substantial Phanerozoic crustal accretion within the Central Asian Orogenic Belt (Wu et al., 2000; Jahn et al., 2004).

Despite progress in geochronological and geochemical studies, the petrogenetic mechanisms and tectonic settings of granitoids in the Lesser Xing'an-Zhangguangcai Range remain contentious (Wu et al., 2011; Ge et al., 2017; Ge et al., 2018; Ge et al., 2019; Zhu C. Y. et al., 2017). Three main models have been proposed to explain magmatism in the Songnen Block: (1) post-subduction or collisional extension following the closure of the Paleo-Asian Ocean (Guo et al., 2018; Long et al., 2020a; Long et al., 2020b); (2) mantle wedge or crustal melting triggered by subduction of the Paleo-Pacific Plate (Ge et al., 2018; Yu et al., 2013); and (3) crustal thickening due to the collision between the Songnen and Jiamusi blocks (Zhu et al., 2017b; Dong et al., 2017; Dong, 2018). However, there is no consensus regarding which tectonic processes play a dominant role. This study investigated the Early Jurassic syenogranite from the northern Zhangguangcai Range through integrated petrological, geochronological, geochemical, and Lu-Hf isotopic analyses to constrain its petrogenesis and tectonic setting. The results could contribute to refining our understanding of the Mesozoic tectonic evolution mechanisms in Northeast China.

2 Geological background

The Xingmeng Orogenic Belt in northern China is a key segment of the Central Asian Orogenic Belt, forming a tectonic connection between the Siberian Plate and North China Plate (Figure 1a). From the Paleozoic to the Mesozoic era, this region experienced a series of tectonic events, including collision, subduction, and metamorphism, among several micro-blocks, such as the Erguna, Xing'an, Songnen, Jiamusi, Khanka, and Nadanhada terranes, ultimately shaping a complex tectonic framework (Figure 1b) (Şengör et al., 1993). This study focused on the Zhangguangcai Range tectonic belt, which is situated in the eastern portion of the Xingmeng Orogenic Belt. The Dun-Mi Fault defines the southern boundary of the block. While early scholars believed that the region contained an ancient Proterozoic metamorphic crystalline basement (Jilin Bureau of Geology and Mineral Resources, 1988; Heilongjiang Bureau of Geology and Mineral Resources, 1993), recent chronological evidence has indicated that the majority of these geological units, previously considered Precambrian, were primarily formed during the Paleozoic and early Mesozoic periods (Wang F. et al., 2017; Feng et al., 2019; Xu et al., 2019), with only a small number dating to the Neoproterozoic (Quan et al., 2013; Wang et al., 2014).

The study area is characterized by the extensive presence of Paleozoic to Early Mesozoic intrusive rocks (Dong, 2018). During the Early Jurassic, vigorous magmatic activity, predominantly felsic in nature, led to the widespread formation of granites, mainly syenogranites, which exhibit a northeast-trending distribution (Figure 2). The exposed strata in the region are primarily represented by the Neoproterozoic Hongguang Formation, a shallow marine marginal clastic sequence composed of metamorphosed intermediate to intermediate-basic volcanic rocks interbedded with phyllite, slate, two-mica schist, and marble. Additionally, the Quaternary strata are extensively developed along the Songhua River within the study area.

3 Samples and analytical techniques

3.1 Lithofacies characteristics of samples

The syenogranites in the study area are extensively distributed and appear as stocks in the field, with exposed plutons primarily consisting of slightly weathered and altered fine-to medium-grained syenogranites. Their mineral composition is predominantly potassium feldspar (50%–55%), plagioclase (20%), quartz (25%), and a minor amount of biotite (2%–3%) (Figure 3). Potassium feldspar, mainly microcline and orthoclase, forms subhedral plates, typically 2–5 mm in size, with some intergrown quartz in graphic textures and sodic stripes arranged in a dendritic pattern. A

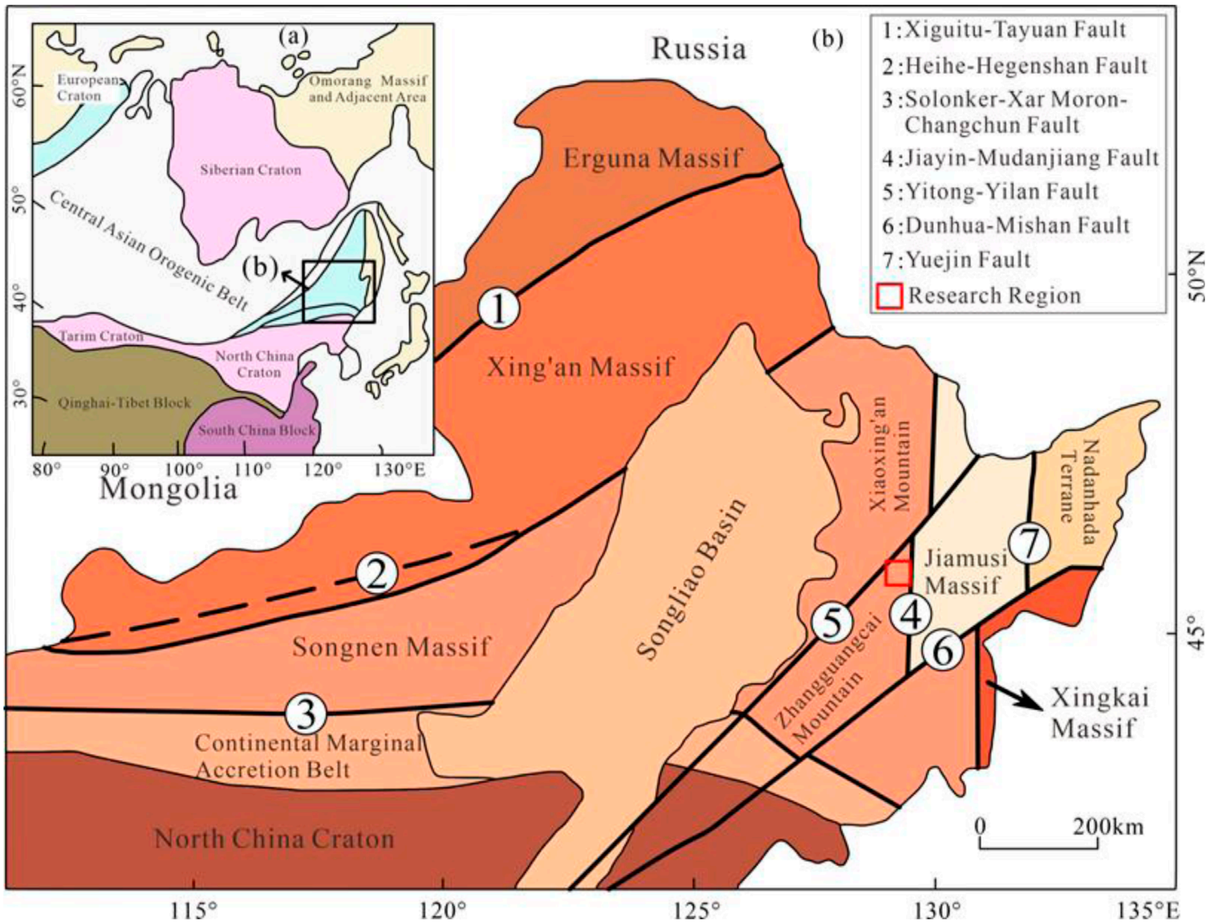

FIGURE 1
Simplified tectonic map **(a)** and geological sketch map **(b)** of the study area (Xu et al., 2019).

few fine plagioclase crystals are embedded within the potassium feldspar, and local plagioclase alteration is present. Plagioclase forms subhedral plates 2–4 mm in size, showing sericitization and weak polysynthetic twinning. Quartz occurs as anhedral grains, generally 2–4 mm in size, with a random distribution, clean surfaces, and light-wavy extinction. Biotite appears as flakes, randomly distributed, with flake sizes ranging from 0.2 to 1.3 mm.

3.2 Analytical methods

3.2.1 Zircon U–Pb dating

U-Pb dating analyses were conducted using LA-ICP-MS at Beijing Createch Testing Technology Co., Ltd., following the operational procedures described by Hou, 2009. Laser sampling was performed using a 193 nm laser ablation system, and the ion signal intensities were measured using an Analytik Jena PQMS Elite ICP-MS instrument. Helium served as the carrier gas, whereas argon was utilized as the makeup gas and combined with the carrier gas through a T-connector before entering the ICP. Each analysis included a background acquisition phase of approximately 15–20 s (gas blank) followed by 45 s of data acquisition from the sample. Data processing, including raw data selection, background and analyte signal integration, time-drift correction, and quantitative calibration for U-Pb dating, was conducted offline using LADR_1.1.07 (Norris and Danyushevsky, 2018).

Zircon GJ-1 was employed as the external standard for U-Pb dating and analyzed twice for every 5–10 sample analyses. The time-dependent drifts in the U-Th-Pb isotopic ratios were corrected *via* linear interpolation, based on the variation observed in the GJ-1 standards (i.e., 2 GJ-1 zircons + 5–10 samples +2 GJ-1 zircons). The uncertainty in the preferred values for GJ-1 was propagated to the final sample results. Common Pb correction was unnecessary for all analyzed zircon grains because of the low ^{204}Pb signal and high ^{206}Pb/^{204}Pb ratios. The U, Th, and Pb concentrations were calibrated using NIST 610. Concordia diagrams and weighted mean age calculations were generated using IsoPlot 4.15. The zircon Plešovice analyzed as an unknown sample yielded a weighted mean ^{206}Pb/^{238}U age of 337.4 ± 1.8 Ma (n = 7, 2SD), which could be consistent with its recommended age of 337.13 ± 0.37 Ma (2SD) (Sláma et al., 2008).

3.2.2 Whole-rock major and trace element analysis

Major and trace element analyses were conducted at the Analysis and Testing laboratory of the Harbin Center for Integrated

10.3389/feart.2025.1578301

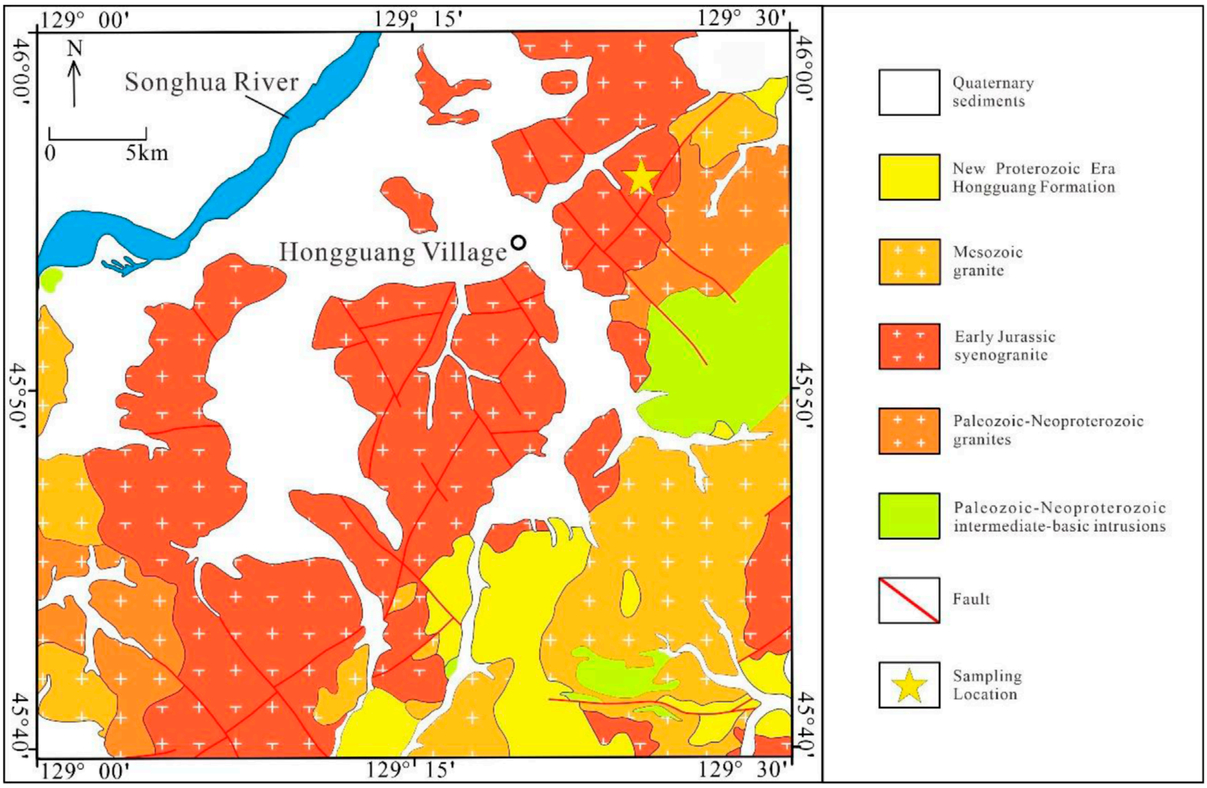

FIGURE 2
Simplified tectonic maps of the study area.

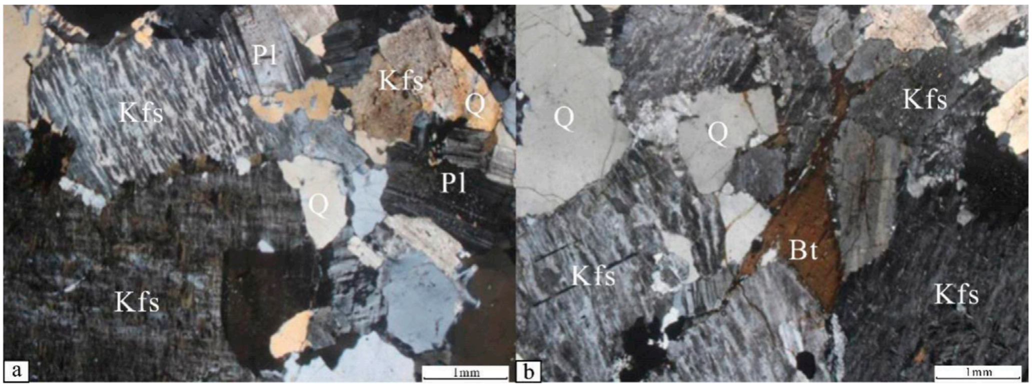

FIGURE 3
Hand specimen **(a)** and microphotographs **(b)** of syenogranite in the study area. Abbreviations: Kfs—K feldspar; Pl—plagioclase; Q—quartz; Bt—biotite.

Natural Resources Survey and China Geological Survey. Fresh rock samples were processed using an agate, contamination-free grinding system to a fineness of 200 mesh and then divided into two portions: approximately 15 g sealed in a white polyethylene bottle for XRF analysis and a 50 mg portion for ICP-MS analysis. Major elements were determined using X-ray fluorescence spectrometry (XRF) with an AXIOSMAX spectrometer from Malvern Panalytical utilizing the instrument's built-in quantitative analysis software with an analytical accuracy generally exceeding 5%. Trace elements were analyzed using a Thermo Fisher XSERIES II ICP-MS instrument, where the solutions were introduced into the high-temperature plasma, and element concentrations were automatically calculated by the mass spectrometer, with an analytical error typically below 5%.

3.2.3 Lu-Hf isotopes of zircon

Hf isotope measurements of zircon micro-areas were performed at the Beijing Createch Testing Technology Co., Ltd. using a

10.3389/feart.2025.1578301

TABLE 1 LA-ICP-MS zircon U-Pb dating data of syenogranite in the study area.

Sample numbers	Th	U	Th/U	Isotope Atomic ratio						Isotopic age (Ma)					
	(10^{-6})			$^{207}Pb/^{206}Pb$	1σ	$^{207}Pb/^{235}U$	1σ	$^{206}Pb/^{238}U$	1σ	$^{207}Pb/^{206}Pb$	1σ	$^{207}Pb/^{235}U$	1σ	$^{206}Pb/^{238}U$	1σ
SHD0042-1	153.38	402.29	0.38	0.05009	0.00140	0.21294	0.00668	0.03100	0.00033	198	6	196	6	197	2
SHD0042-2	159.49	366.21	0.44	0.04927	0.00164	0.20568	0.00714	0.03044	0.00030	160	5	190	7	193	2
SHD0042-3	197.48	379.59	0.52	0.04912	0.00153	0.21231	0.00695	0.03146	0.00028	152	5	195	6	200	2
SHD0042-4	312.93	644.74	0.49	0.05139	0.00117	0.21282	0.00515	0.03016	0.00024	257	6	196	5	192	2
SHD0042-5	113.44	259.66	0.44	0.05254	0.00200	0.22504	0.00915	0.03116	0.00034	308	12	206	8	198	2
SHD0042-6	306.65	561.33	0.55	0.04961	0.00144	0.20661	0.00616	0.03035	0.00024	176	5	191	6	193	2
SHD0042-7	384.81	699.96	0.55	0.04960	0.00113	0.20528	0.00534	0.03018	0.00024	175	4	190	5	192	2
SHD0042-8	211.80	492.51	0.43	0.05070	0.00144	0.21490	0.00639	0.03094	0.00028	226	6	198	6	196	2
SHD0042-9	119.93	249.00	0.48	0.05484	0.00181	0.22726	0.00747	0.03029	0.00033	405	13	208	7	192	2
SHD0042-10	194.85	377.52	0.52	0.05072	0.00140	0.21683	0.00618	0.03129	0.00029	227	6	199	6	199	2
SHD0042-11	161.75	361.41	0.45	0.05117	0.00161	0.21237	0.00709	0.03043	0.00032	247	8	196	7	193	2
SHD0042-12	136.62	300.86	0.45	0.05136	0.00179	0.21407	0.00799	0.03050	0.00031	256	9	197	7	194	2
SHD0042-13	166.12	348.72	0.48	0.04886	0.00151	0.20361	0.00658	0.03049	0.00029	140	4	188	6	194	2
SHD0042-14	219.49	454.95	0.48	0.05134	0.00153	0.21463	0.00642	0.03057	0.00029	255	8	197	6	194	2
SHD0042-15	220.27	624.03	0.35	0.04886	0.00113	0.20566	0.00540	0.03076	0.00028	140	3	190	5	195	2
SHD0042-16	172.03	372.70	0.46	0.04866	0.00159	0.20179	0.00695	0.03030	0.00031	130	4	187	6	192	2
SHD0042-17	248.67	463.72	0.54	0.05356	0.00139	0.22306	0.00641	0.03045	0.00026	352	9	204	6	193	2
SHD0042-18	222.39	456.19	0.49	0.05099	0.00161	0.21226	0.00697	0.03038	0.00028	240	8	195	6	193	2
SHD0042-19	128.58	295.67	0.43	0.05259	0.00190	0.21810	0.00805	0.03035	0.00031	310	11	200	7	193	2
SHD0042-20	139.05	299.34	0.46	0.05120	0.00193	0.21539	0.00808	0.03077	0.00029	249	9	198	7	195	2

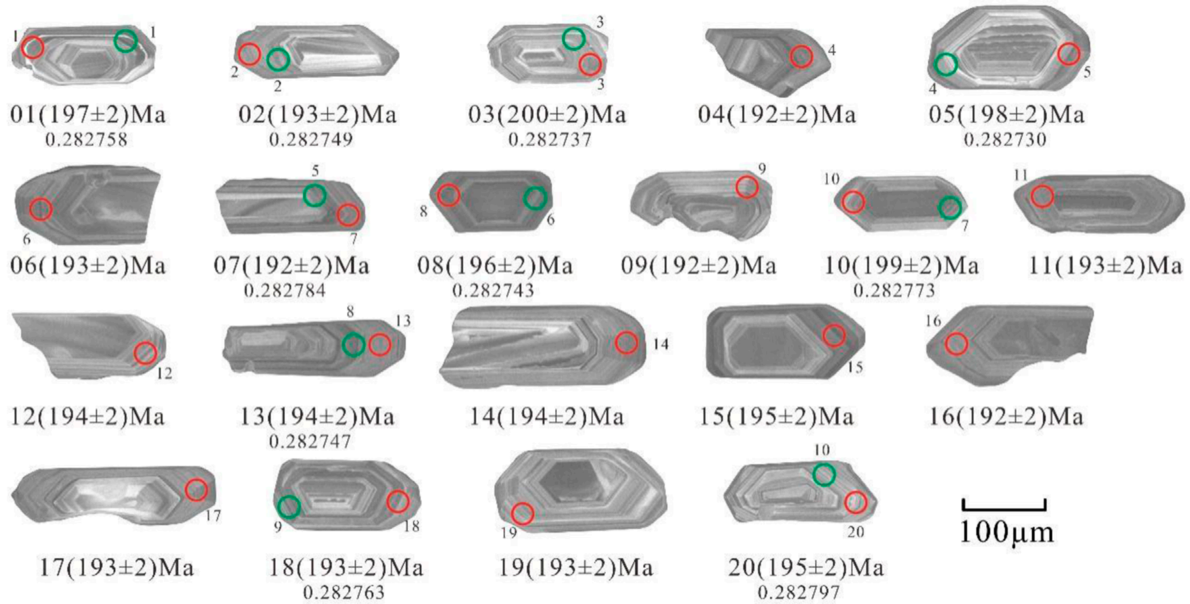

FIGURE 4
Zircon cathodoluminescence diagram of syenogranite in the study area. The red circle is the U-Pb dating position, the green circle is the Lu-Hf isotope analysis position, and the number represents the analysis point number. The ages and $^{176}Hf/^{177}Hf$ isotope ratios of the test points are labeled below.

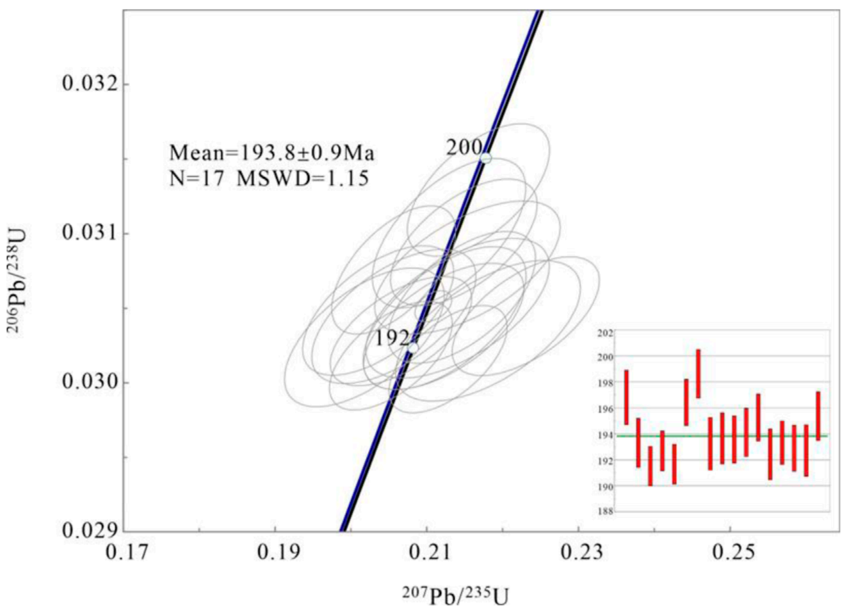

FIGURE 5
Zircon LA-ICP-MS U-Pb concordia diagram from syenogranite in the study area.

laser ablation multi-collector inductively coupled plasma mass spectrometer. The analysis employed a RESOlution-SE solid-state laser ablation system coupled with a NEPTUNE Plus multi-collector plasma mass spectrometer. Internal zircon structures were observed using cathodoluminescence (CL) imaging to select precise analytical spots. Laser ablation was performed for a duration of 27 s, spot diameter of approximately 30 μm, energy density of 6 J/cm^2, and frequency of 6 Hz. The Plešovice zircon standard was used as a calibration reference to ensure the analytical accuracy. The measured $^{176}Hf/^{177}Hf$

TABLE 2 Major (wt%) and trace ($\times10^{-6}$) elements compositions of syenogranite in the study.

Sample numbers	SHD0041	SHD0736	SHD0749	SHD0909	SHD0748	SHD0731	SHD0803
SiO_2	70.59	72.59	73.39	73.62	74.62	74.87	76.81
TiO_2	0.21	0.14	0.17	0.17	0.06	0.07	0.12
Al_2O_3	14.72	12.58	12.07	12.11	12.33	11.37	10.92
FeO	0.69	1.68	0.71	0.55	0.52	0.69	0.63
Fe_2O_3	1.46	0.05	0.56	1.08	0.13	0.28	0.34
MnO	0.05	0.04	0.03	0.06	0.03	0.02	0.03
MgO	0.38	0.23	0.21	0.22	0.06	0.07	0.08
CaO	1.66	0.98	0.90	0.56	0.49	0.28	0.39
Na_2O	3.88	3.86	3.49	3.80	4.10	3.10	3.34
K_2O	4.34	4.17	4.35	4.24	4.18	5.28	4.31
P_2O_5	0.10	0.04	0.04	0.06	0.02	0.02	0.02
LOI	0.89	0.03	0.37	1.61	0.12	0.26	0.29
TOTAL	98.96	96.38	96.29	98.07	96.65	96.32	97.28
δ	2.45	2.18	2.02	2.11	2.17	2.20	1.73
A/CNK	1.04	0.99	1.00	1.02	1.01	1.00	1.00
A/NK	1.33	1.16	1.15	1.12	1.09	1.05	1.07
TFeO	2.00	1.72	1.21	1.52	0.64	0.94	0.94
TFeO/(TFeO + MgO)	0.84	0.88	0.85	0.87	0.91	0.93	0.92
$Na_2O + K_2O$	8.22	8.03	7.84	8.04	8.28	8.38	7.65
K_2O/Na_2O	1.12	1.08	1.25	1.12	1.02	1.70	1.29
DI	96	96	98	97	98	98	98
La	31.1	36	37.6	15.2	15.2	20.9	22.5
Ce	56.2	68.5	73.9	74.7	31.3	38.1	36.8
Pr	5	5.98	6.18	3.34	3.4	3.65	4.02
Nd	19.2	24.2	24.4	13.7	13.8	14	15
Sm	2.73	4.23	3.86	3.36	2.67	2.01	2.49
Eu	0.94	0.47	0.78	0.42	0.64	0.31	0.3
Gd	2.83	3.91	3.8	3.31	2.38	2.13	2.44
Tb	0.34	0.55	0.51	0.57	0.34	0.25	0.36
Dy	1.99	3.16	2.97	3.89	2.14	1.58	2.4
Ho	0.41	0.65	0.62	0.83	0.43	0.33	0.54
Er	1.18	1.82	1.83	2.57	1.2	0.89	1.7
Tm	0.22	0.33	0.34	0.5	0.23	0.17	0.34

(Continued on the following page)

TABLE 2 (*Continued*) Major (wt%) and trace (x10^{-6}) elements compositions of syenogranite in the study.

Sample numbers	SHD0041	SHD0736	SHD0749	SHD0909	SHD0748	SHD0731	SHD0803
Yb	1.38	2.03	2.12	3.23	1.36	1.05	2.16
Lu	0.23	0.32	0.33	0.51	0.22	0.18	0.32
Y	11.1	15.4	15.3	26.5	11.9	8.77	13.6
ΣREE	123.75	152.15	159.24	126.13	75.31	85.55	91.37
LREE	115.17	139.38	146.72	110.72	67.01	78.97	81.11
HREE	8.58	12.77	12.52	15.41	8.3	6.58	10.26
LREE/HREE	13.42	10.91	11.72	7.18	8.07	12.00	7.91
La_N/Yb_N	16.17	12.72	12.72	3.38	8.02	14.28	7.47
δEu	1.03	0.35	0.62	0.38	0.76	0.45	0.37
Li	8.57	19.4	16.1	14.1	7.05	1.24	4.59
Be	1.9	1.53	1.7	5.02	1.06	0.52	2.13
Sc	1.37	3.15	2.26	2.12	1.2	1.44	1.62
V	13.5	8.06	12.7	8.95	5.61	6.36	5.87
Cr	17.4	20.1	28.8	22.8	14.7	25.4	24.9
Co.	2.92	2.52	2.19	3.05	1.15	1.58	1.46
Ni	<2	<2	2.17	4.6	<2	4	<2
Cu	2.86	6.78	2.99	14.4	3.68	4.46	3.17
Zn	46.9	40.5	22.1	37	12.1	16.7	14.1
Ga	17.2	17.2	14.2	17.4	15.7	15.9	14.8
Rb	127	101	114	179	97.6	131	176
Sr	404	127	121	74.9	104	31.7	28.4
Zr	153	173	105	143	45.3	94.8	81.4
Nb	7.72	6.88	8.15	23.3	9.93	4.08	9.46
Mo	0.22	0.68	0.22	0.31	0.31	0.33	0.47
Ba	1213	634	586	342	1029	279	128
Hf	3.69	5.98	6.21	9.85	17.8	2.65	6.27
Ta	0.78	0.71	0.88	2.14	0.84	0.56	1.1
W	9.64	9.4	5.98	8.02	6.76	5.9	6.52
Pb	25	22.2	14.5	18	27.6	19.2	15.9
Bi	0.058	0.076	0.1	0.98	<0.05	0.11	<0.05
Th	9.97	11.2	10.2	28.6	5.11	5.37	20
Ag	0.024	0.027	0.024	0.053	0.026	0.047	0.023
Sn	2	2.2	1.6	1.78	1.4	1.26	1.46

(Continued on the following page)

TABLE 2 (*Continued*) Major (wt%) and trace ($\times10^{-6}$) elements compositions of syenogranite in the study.

Sample numbers	SHD0041	SHD0736	SHD0749	SHD0909	SHD0748	SHD0731	SHD0803
B	3.06	8.06	4.15	7.99	3.56	3.12	2.89
Hg	0.005	0.004	0.005	0.006	0.004	0.005	0.005
F	275	246	256	163	150	101	185
Cl	67.3	67.3	38.2	57	35.8	42.2	41.6

ratio remained stable at 0.282488 ± 20 (2SD, n = 6), which is consistent with the values reported by Sláma et al. (2008) within acceptable error margins.

4 Results

4.1 Zircon U–Pb geochronology

The LA-ICP-MS zircon U-Pb dating results for the syenogranite samples from the study area are presented in Table 1. Under a microscope, the selected zircons predominantly appeared as well-formed, colorless, translucent crystals with short-to long-columnar habits (Figure 4), exhibiting long axis lengths ranging from 60 to 220 μm and aspect ratios between 1.5:1 and 4:1. Most zircon grains displayed distinct and consistent oscillatory zoning, characteristic of magmatic origin, without sharp core-rim boundaries but with gradually increasing zoning density from core to rim, possibly reflecting the variations in the crystal growth rates during magma cooling. A few zircons demonstrated clear core-rim structures, likely representing inherited cores from earlier geological events that experienced partial hydrothermal or solid-state recrystallization during subsequent magmatic activity (Gong et al., 2009). The high Th/U ratios of 0.35–0.55 further support their magmatic origin (Rubatto, 2002; Wu and Zheng, 2004).

All 20 zircon analysis points from the syenogranite sample exhibited good concordance, aligning closely with the U-Pb concordia line (Figure 5), indicating no significant lead loss or post-crystallization isotopic disturbance. The weighted average $^{206}Pb/^{238}U$ age was calculated to be 194 ± 2 Ma (Figure 5), representing the formation age of the pluton.

4.2 Whole-rock major and trace elements

The whole-rock major and trace element results for the seven syenogranite samples are summarized in Table 2. The major element compositions exhibited limited variability, with SiO_2 ranging from 70.59% to 76.81%, Al_2O_3 from 10.92% to 14.72%, K_2O from 4.17% to 5.28%, and Na_2O from 3.1% to 4.1%. The TiO_2, MnO, and P_2O_5 contents were all below 1%, and the loss on ignition (LOI) values ranged from 0.03% to 1.61%, suggesting a minimal influence of late-stage alteration or fluid activity and preservation of the original geochemical signatures. The aluminum saturation index (A/CNK) ranged from 0.99 to 1.04, averaging 1.02, placing the samples in the metaluminous to weakly peraluminous fields on the A/NK-A/CNK diagram (Figure 6a). The K_2O/SiO_2 ratio ranged from 0.06 to 0.07, averaging 0.06, and the samples plotted within the high-K calc-alkaline series on the K_2O-SiO_2 diagram (Figure 6b). In the TAS and QAP classification diagrams for intrusive rocks (Figures 6d,e), all the samples fell within the granite field, whereas in the R1-R2 diagram (Figure 6c), they were located within or near the syenogranite field. The Rittmann index ($\sigma = (Na_2O + K_2O)^2/(SiO_2$-43)) ranged from 1.73 to 2.45, confirming their classification as calc-alkaline granite.

The total rare earth element (REE) content of the samples was relatively low, ranging from 75.31 to 159.24 ppm. In the chondrite-normalized REE diagram (Figure 7), the samples exhibited a right-leaning distribution pattern with $(La/Yb)_N$ values from 3.38 to 16.17, indicating enrichment in light rare earth elements (LREEs) (67.01–146.72 ppm) and depletion in heavy rare earth elements (HREEs) (6.58–15.41 ppm), along with a relatively weak negative europium anomaly (δEu = 0.35–1.03). In the primitive mantle-normalized trace element diagram (Figure 7), the samples displayed consistent distribution patterns, showing the enrichment in large ion lithophile elements (LILEs) such as Rb and K, and the depletion in high field strength elements (HFSEs) including Nb, Ta, and Ti. Additionally, the samples exhibited varying degrees of Ba depletion and significant depletion in Sr and P.

4.3 Hf isotope characteristics

The Lu-Hf isotope results for zircon in Table 3 present minimal variation in $^{176}Hf/^{177}Hf$ value (0.282730–0.282797), indicating the strong isotopic consistency. The analyzed zircons exhibited relatively low $^{176}Lu/^{177}Hf$ ratios (0.001164–0.002033), mostly below or near 0.002, suggesting minimal radiogenic Hf accumulation since formation and confirming that the measured $^{176}Hf/^{177}Hf$ ratios accurately represent the Hf isotopic composition at the time of zircon crystallization (Amelin et al., 1999). Additionally, the $f_{Lu/Hf}$ values ranged from −0.96 to −0.94, significantly lower than those of mafic crust (−0.34) and felsic crust (−0.72) (Vervoort et al., 1996; Amelin et al., 2000), indicating that the two-stage Hf model age could provide a reliable estimate of the magma source's initial separation time or its average crustal residence age (Liu et al., 2014). The $\varepsilon_{Hf}(t)$ values of sample SHD0042 ranged from +2.7 to +5.0, with corresponding depleted mantle two-stage model ages (T_{DM2}) between 915 and 1067 Ma.

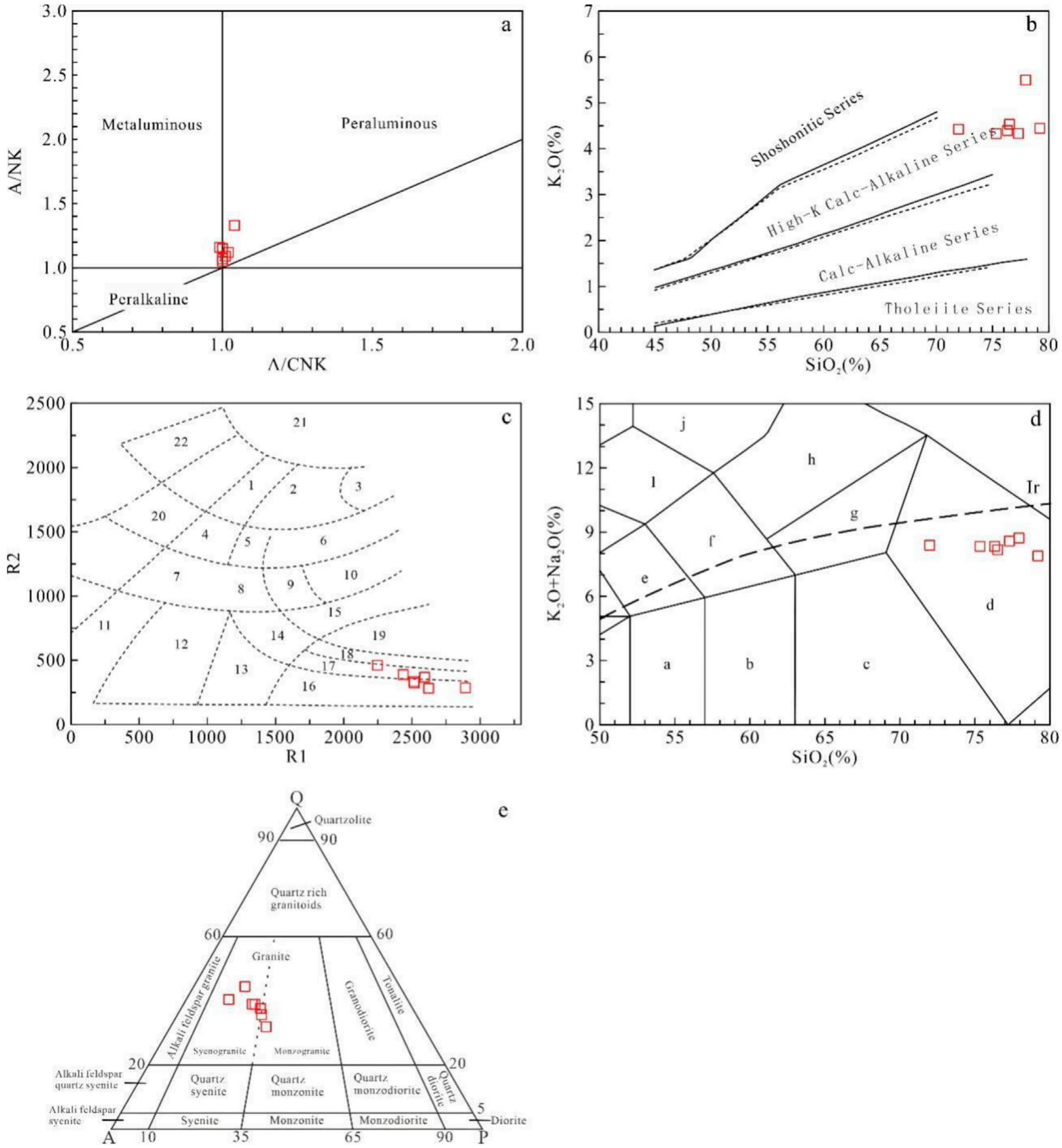

FIGURE 6
A/NK vs. A/CNK diagram (Maniar and Piccoli, 1989) **(a)**, SiO_2 vs.K_2O diagram (Peccerillo and Taylor,1976) **(b)**, R1-R2 diagram (De La Roche et al., 1980) **(c)**, TAS diagram (Middlemost, 1994) **(d)** and QAP diagram (Streckeisen, 1973) **(e)** of syenogranite in the study area. 1—Alkaline Gabbro; 2—Olivine Gabbro; 3—Gabbro Syenite; 4—Monzonitic Gabbro; 5—Dioritic Gabbro; 6—Gabbro; 7—Monzonite; 8—Monzonite; 9—Monzodiorite; 10—Diorite; 11—Nepheline Syenite; 12—Syenite; 13—Quartz Syenite; 14—Quartz Monzonite; 15—Tonalite; 16—Alkali Granite; 17—Syenogranite; 18—Monzograiite; 19—Granodiorite; 20—Essexite; 21—Peridotite; 22—Ijolite; a—Gabbroic Diorite; b—Diorite; c—Granodiorite; d—Granite; e—Monzodiorite; f—Monzosyenite; g—Quartz Monzonite; h—Syenite; i—Foid Monzosyenite; j—Foidolite Syenite.

5 Discussion

5.1 Jurassic magmatism in the Zhangguangcai Range orogenic belt

The Zhangguangcai Range preserves evidence of intense Late Paleozoic to Early Mesozoic magmatism, notably marked by extensive ~190 Ma granitic plutons comprising granodiorite, monzogranite, syenogranite, and alkali feldspar granite. These granitoids exhibit characteristic I-type features (Liu et al., 2016; Liu et al., 2017; Ge et al., 2017; Ge et al., 2018) and were interpreted by Wu et al. (2003a), Wu et al. (2003b) as highly fractionated products of prolonged crystal differentiation. Petrogenetic models suggest that their magmas originated either from juvenile crustal melting (Xu M. J. et al., 2013; Li et al., 2016) or mantle-crust magma mixing (Ren, 2019). In contrast, mafic magmatism is spatially and temporally limited, represented by several suites: the Xinxinglinchang

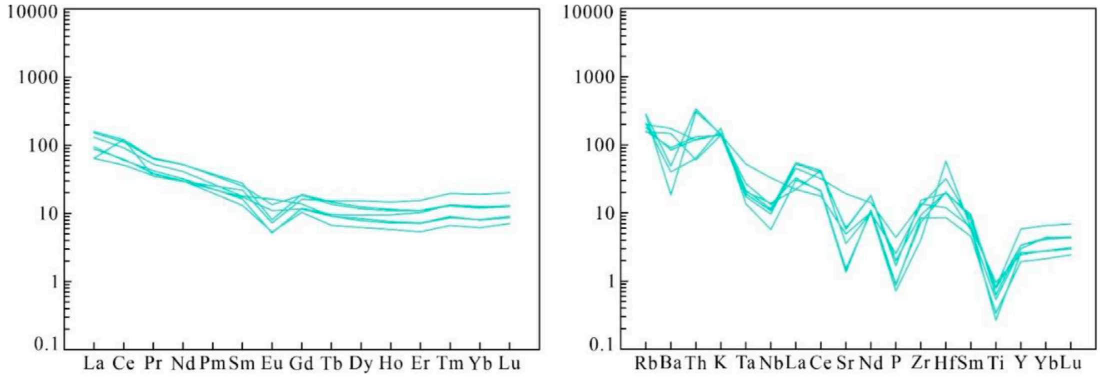

FIGURE 7
Chondrite-normalized REE distribution patterns diagram and primitive mantle-normalized trace element patterns diagram of syenogranite in the study area (Sun and McDonough, 1989).

gabbro (293 Ma; Long et al., 2020a), Hongguang Formation gabbro-diorite (259 Ma; Wang et al., 2012), Shuguanglinchang hornblende gabbro (215 Ma) and gabbro (210 Ma; Long et al., 2020b), and Tangwanghe-Yichun-Mulan gabbro-gabbro-diorite-amphibolite suite (186–182 Ma; Yu et al., 2012). Early Jurassic mafic rocks (Yu et al., 2012; Ge et al., 2020a) exhibit zircon Hf isotopic and geochemical signatures indicative of derivation from partial melting of the subduction-fluid-metasomatized depleted mantle. Comparative analyses revealed contrasting mantle sources: Lesser Xing'an-Zhangguangcai mafic rocks reflect deep-sea sediment contributions, while their Yanbian counterparts can be characterized by terrestrial sediment-dominated sources (Zhao et al., 2018).

The spatiotemporal evolution of intrusive rocks in the Lesser Xing'an–Zhangguangcai Range provides critical insights into the tectonic evolution of the region. By integrating regional zircon U-Pb geochronological datasets, this study confirmed that Early Mesozoic magmatism peaked during the Early Jurassic (180–200 Ma) (Supplementary Table S1; Figure 8a). These intrusive rocks were primarily concentrated between 127° and 130°E (Figure 8b), forming a prominent north-south-trending magmatic belt. Importantly, Early Mesozoic intrusive rocks exhibited distinct spatiotemporal patterns. After accounting for strike-slip displacement along the Yitong-Yilan Fault (a northern extension of the Tanlu Fault Zone) and categorizing the data into north and south of the fault, our study identified a westward-younging magmatic migration trend (Figure 8b). This finding reinforces previous models of westward migration of magmatic activity based on granite data (Ge et al., 2020b) and extends their applicability by including chronological evidence from intermediate-mafic intrusions. The syenogranite dated in this study yielded a zircon LA-ICP-MS U-Pb weighted mean age of 194 ± 2 Ma, with zircon grains showing typical magmatic growth zoning and Th/U ratios between 0.35 and 0.55. The narrow age range of 8 Ma among all the analyzed points indicated that the syenogranite was emplaced in the early Jurassic. Together with regional data, these results confirmed that extensive magmatism occurred in the Lesser Xing'an-Zhangguangcai Range during the Early Jurassic.

5.2 Petrogenesis of the syenogranites

Most sample points on the genetic discriminant diagrams fell within the I- and S-type granite fields, with only a few near the boundary separating the A-type from the I-and S-type granites (Figures 9a,b). Based on the zircon saturation temperature calculation method of Watson and Harrison (1983), the syenogranites yielded temperatures between 688°C and 791°C, which were significantly lower than the typical formation temperatures of A-type granites (>900°C) (Eby, 1992), indicating that the studied rocks were not A-type granites. Additionally, the samples showed only a slight negative Eu anomaly, in contrast to the strongly negative Eu anomaly generally observed in the A-type granites. Microscopic analysis revealed no alkali-rich minerals, such as riebeckite or aegirine, and the plagioclase content was relatively high. Both features were inconsistent with the A-type granite mineralogy (Chappell, 1999), further confirming that the syenogranites were not of A-type affinity.

The S-type granite magmas generally originated from phosphorus-rich sedimentary rocks, where phosphorus cannot be fully incorporated into minerals during magmatic evolution, resulting in simultaneous increases in SiO_2 and P_2O_5 contents. In contrast, the I-type granite magmas were derived from crustal mafic rocks or mantle materials, with phosphorus being progressively excluded as the SiO_2 content increased and the P_2O_5 content decreased. This trend is consistent with the granite characteristics observed in the study area (Figure 10) (Chappell, 1999; Qiu et al., 2024). Moreover, the complete absence of aluminum-rich minerals such as garnet, muscovite, tourmaline, and cordierite, coupled with the weakly peraluminous nature (A/CNK = 0.99–1.04) and the positive correlation between Rb and Th, further supported the interpretation that the syenogranites were not S-type but belonged to the I-type granite category (Figure 9d) (Qiu et al., 2008).

The rock samples displayed a high SiO_2 content (>70%), elevated K_2O/Na_2O ratios (>1), enrichment in large ion lithophile elements (LILE) such as K and Rb, and depletion in high field strength elements (HFSE), including Nb, Ta, and Ti. These geochemical features, combined with the high differentiation indices (DI = 96–98), were consistent with the traits of the highly

10.3389/feart.2025.1578301

TABLE 3 Zircon Hf isotopic analysis results of syenogranite in the study area.

Sample	Age (Ma)	$^{176}Yb/^{177}Hf$	2σ	$^{176}Lu/^{177}Hf$	2σ	$^{176}Hf/^{177}Hf$	2σ	ε_{Hf} (0)	ε_{Hf} (t)	$f_{Lu/Hf}$	T_{DM1} (Ma)	T_{DM2} (Ma)
SHD0042-1	196.8	0.039224	0.000740	0.001294	0.000019	0.282758	0.000015	−0.5	3.7	−0.96	705	1003
SHD0042-2	193.3	0.048792	0.000774	0.001646	0.000031	0.282749	0.000017	−0.8	3.2	−0.95	726	1029
SHD0042-3	199.7	0.035343	0.000435	0.001199	0.000012	0.282737	0.000017	−1.2	3.0	−0.96	733	1048
SHD0042-5	197.8	0.036630	0.000817	0.001236	0.000023	0.282730	0.000016	−1.5	2.7	−0.96	745	1067
SHD0042-7	191.7	0.057538	0.001805	0.001943	0.000066	0.282784	0.000017	0.4	4.4	−0.94	680	953
SHD0042-8	196.4	0.060789	0.001077	0.002033	0.000035	0.282743	0.000019	−1.0	3.0	−0.94	741	1043
SHD0042-10	198.6	0.050640	0.000371	0.001732	0.000019	0.282773	0.000017	0.0	4.2	−0.95	692	972
SHD0042-13	193.6	0.038603	0.000119	0.001272	0.000003	0.282747	0.000015	−0.9	3.2	−0.96	720	1030
SHD0042-18	192.9	0.047680	0.000336	0.001648	0.000008	0.282763	0.000017	−0.3	3.7	−0.95	705	998
SHD0042-20	195.4	0.034194	0.000863	0.001164	0.000027	0.282797	0.000016	0.9	5.0	−0.96	648	915

fractionated I-type granites (Wang Z. Z. et al., 2017). Furthermore, the syenogranite sample points plotted on the TFeO/MgO-Zr + Nb + Ce + Y (Figure 9b) and (Al_2O_3+CaO)/TFeO + K_2O + Na_2O−100×(MgO + TFeO + TiO_2)/SiO_2 diagrams (Figure 9c) were situated within the highly fractionated field. Thus, based on their geochemical and mineralogical characteristics, the syenogranites in the study area were identified as highly fractionated I-type granites.

5.2.1 Fractional crystallization process

The samples displayed a right-leaning rare earth element (REE) distribution pattern characterized by relative enrichment in light rare earth elements (LREEs) and depletion in heavy rare earth elements (HREEs), accompanied by a weak negative Eu anomaly. They were enriched in large ion lithophile elements (LILEs) such as Rb and K and depleted in high field strength elements (HFSEs) including Nb, Ta, and Ti, with varying degrees of Ba depletion and notable depletion in Sr and P. The negative Eu anomaly commonly observed in granites is generally attributed to fractional crystallization of plagioclase or retention of plagioclase in the magma source. Sr was concentrated in feldspars through the isomorphous substitution of Ca and Na, whereas Ba was preferentially incorporated into K-rich minerals such as potassium feldspar and biotite during the late stages of magma evolution, occupying K sites in early crystallized K-bearing phases. Consequently, plagioclase fractionation led to Eu-Sr depletion, while the crystallization of potassium feldspar and biotite contributed to Ba depletion and further enhanced the negative Eu anomaly. The negative anomalies of P and Ti were primarily linked to the fractionation of accessory minerals, such as apatite and titanite. Furthermore, because apatite typically displays a negative Eu anomaly (Sha and Chappell, 1999), its separation may partially offset Eu depletion caused by plagioclase fractionation (Qian et al., 2002).

In the Harker diagrams of the samples, increasing SiO_2 content was accompanied by decreasing concentrations of MgO, TiO_2, CaO, TFeO, P_2O_5, and Eu (Figure 10), reflecting the fractional crystallization of various mineral phases during magma evolution. The negative correlations between SiO_2 and TiO_2, TFeO, and P_2O_5, along with the pronounced P and Ti depletion in the primitive mantle-normalized trace element spider diagram (Figure 7), suggested the fractional crystallization of titanomagnetite and apatite. Similarly, the inverse relationships between MgO, CaO, Eu, and SiO_2 indicated that amphibole and plagioclase also underwent fractional crystallization. Overall, these compositional variations in the syenogranites were primarily attributed to fractional crystallization processes.

5.2.2 Characteristics of magma sources

There are three main interpretations of the magma source of highly fractionated high-K calc-alkaline I-type granites: (1) fractional crystallization of mantle-derived basaltic magma (Soesoo, 2000; Li et al., 2007); (2) magma generation through crust-mantle mixing during underplating of mantle-derived magma in the lower crust (Wu et al., 2003a; Wu et al., 2003b; Xia et al., 2015); and (3) partial melting of mafic lower crustal rocks (Chappell and White, 2001). The Early Jurassic granites investigated in this study were widely distributed across the eastern Songnen Block, while the coeval intermediate to mafic rocks were much less extensive, rendering it unlikely that such large volumes of felsic magma formed

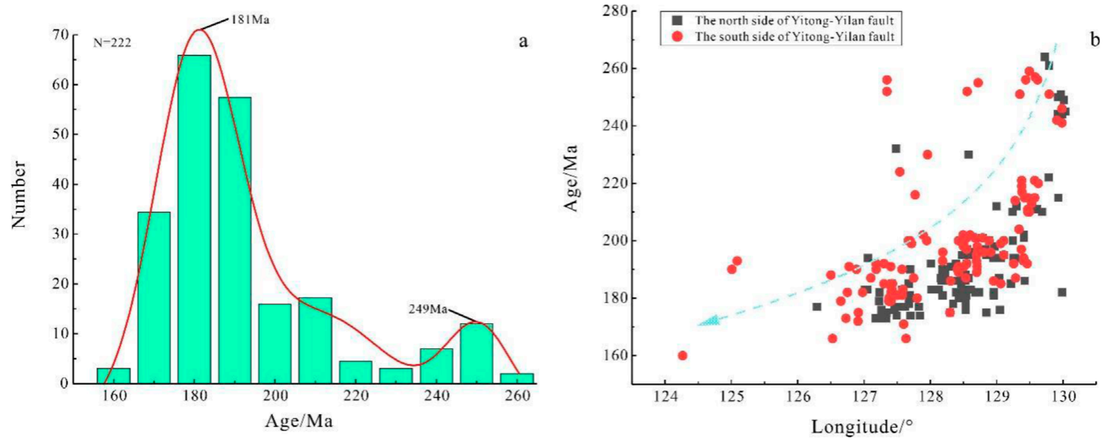

FIGURE 8
Zircon U-Pb ages characterization of intrusive rocks in the Lesser Xing'an- Zhangguangcai Range (**a, b**).

solely through the fractional crystallization of mantle-derived melts. Furthermore, the absence of contemporaneous mafic enclaves and the uniform zircon Hf isotopic compositions indicated that the crust-mantle magma mixing was not the dominant mechanism for syenogranite formation. Geochemical evidence supports a crustal origin for syenogranites. Nb/Ta (7.29–11.82, avg. 9.62), Th/Ta (6.08–18.18, avg. 16.62), and Sm/Nd (0.14–0.24, avg. 0.18) ratios were more consistent with crustal values (Nb/Ta = 11, Th/Ta = 11.67, Sm/Nd = 0.25) (Rudnick and Gao, 2003; Sun and McDonough, 1989; Taylor and McLennan, 1985) than with mantle values (Nb/Ta = 17.5, Th/Ta = 2.3, Sm/Nd = 0.33). The rocks also exhibited high SiO_2, Al_2O_3, and total alkali contents; low MgO levels; the enrichment in K, Rb, and Th; and the depletion in Ba, Nb, Ta, P, and Ti. These could align with the characteristics of crust-derived magmas (Green, 1995; Barth et al., 2000), thereby reinforcing a crustal origin for syenogranites.

Experimental petrological studies have demonstrated that magmas generated by the partial melting of basic rocks typically exhibit low MgO content, low $Mg^{\#}$ values (<40), and depletion of Cr and Ni (Rapp and Watson, 1995). The geochemical characteristics of syenogranite samples from this region (MgO = 0.06–0.38 wt.%, average 0.18; $Mg^{\#}$ = 11.69–25.26, average 18.25; Cr = 14.7–28.8 ppm, average 22.01; Ni < 5 ppm) are highly consistent with this petrogenetic model and overlapped with the major element composition of melts derived from the amphibolite-facies basic rocks in the lower crust (Qian and Hermann, 2013), indicating a source region from partial melting of lower crustal basic rocks. The rare earth element (REE) patterns show the strong fractionation between light and heavy REEs ($(La/Yb)_N$ = 3.38–16.17), low HREE contents (Yb = 1.05–3.23 ppm; Y = 8.77–26.5 ppm), and relatively flat HREE distribution curves ($(Gd/Yb)_N$ = 0.85–1.7). These features are consistent with amphibole as the dominant residual phase, given the high partition coefficient of Yb in felsic melts (Klein et al., 1997), which tends to produce flatter HREE patterns than garnet-bearing systems. This is further supported by the observed Y/Yb ratios (6.3–8.75, average 7.78), which are significantly lower than those typical of garnet-residue systems (Y/Yb > 10) and align more closely with amphibole-controlled systems (≈10) (Rollinson, 1993). Additionally, the samples plotted within the Hf isotopic composition field of the Phanerozoic igneous rocks in the Xingmeng Orogenic Belt on the t vs $\varepsilon_{Hf}(t)$ diagram (Figure 11), with T_{DM2} model ages ranging from 915 to 1067 Ma, indicating a Mesoproterozoic to Neoproterozoic lower crustal source. The consistent Hf isotopic signatures suggest a relatively homogeneous magma source, reinforcing the interpretation that the syenogranites in the study area were primarily derived from the partial melting of amphibolite-facies basic rocks in the juvenile lower crust formed during the Mesoproterozoic to Neoproterozoic.

5.3 Tectonic background

The identification of Early-Middle Triassic collision-type granites along the southern margin of the Xing'an-Mongolian Orogenic Belt provides critical constraints on the timing of the Paleo-Asian Ocean closure, which is estimated to have occurred during the Early-Middle Triassic period. The recognition of Late Triassic bimodal igneous rock assemblages in the Zhangguangcai Range (Wu et al., 2011; Tang et al., 2018; Xu et al., 2019) further supports the interpretation that the Paleo-Asian Ocean could be already closed prior to the Late Triassic period. From the Late Triassic to Early Jurassic, the Mongol-Okhotsk Oceanic Plate subducted beneath the Siberian-Erguna Block in a "scissors-like" closure pattern (Li, 2013; Xu et al., 2019), while the region east of the Songliao Basin was governed by the westward subduction system of the Paleo-Pacific Plate (Xu et al., 2013c; Tang et al., 2018). This tectonic configuration is corroborated by multiple lines of evidence: (1) the widespread presence of Early Jurassic high-K calc-alkaline granite belts in the Yanji-Liaoyuan and Lesser Xing'an-Zhangguangcai Range regions (Zhang et al., 2004; Xue et al., 2024) and (2) the subduction-related geochemical characteristics of Early Jurassic calc-alkaline volcanic rocks in the Jiamusi and Songnen Blocks (Yu et al., 2012; Qin et al., 2016; Wang F. et al., 2017; Wang et al., 2017 Z. H.).

The Mudanjiang Ocean, a paleo-oceanic tectonic unit between the Jiamusi and Songnen Blocks (Wu et al., 2011), has been

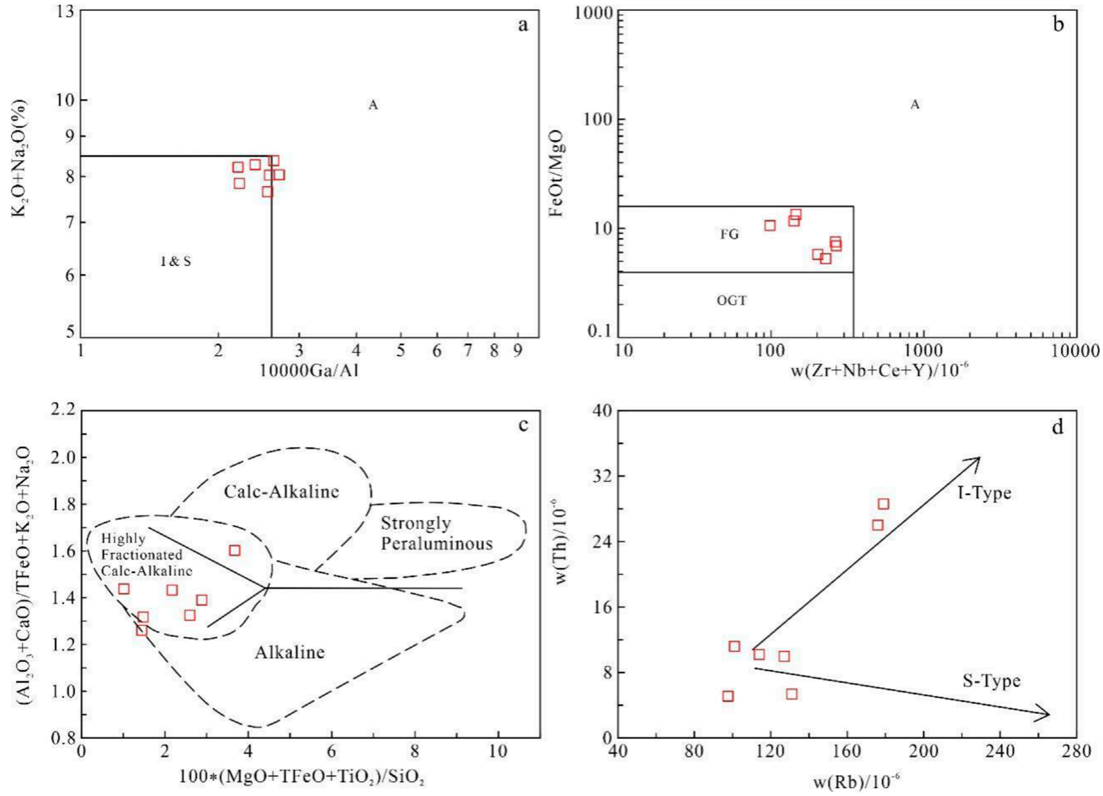

FIGURE 9
Identification of genetic types of syenogranite in the study area (Sylvester, 1989; Whalen et al., 1987) **(a)** $K_2O + N_2O$–Ga/Al diagram; **(b)** TFeO/MgO–Zr + Nb + Ce + Y diagram; **(c)** $(Al_2O_3 + CaO)/TFeO + K_2O + Na_2O$–100*(MgO + TFeO + TiO_2)/SiO_2 diagram; **(d)** Th–Rb diagram.

proposed by previous studies to have existed since at least the Early Permian (Dong et al., 2017; Du et al., 2022; Jing et al., 2022; Yu et al., 2023) and could have evolved continuously as a branch of the Paleo-Pacific Ocean (Sun et al., 2015; Yang et al., 2015; 2019; Yu et al., 2023). The protolith records of OIB-MORB-type blueschists in the Heilongjiang Complex (Jing et al., 2022) together with regional arc magmatic rock belts provide robust constraints on the occurrence of subduction in the Mudanjiang Ocean during the Early Mesozoic. The key supporting evidence includes: (1) Middle-Late Permian arc-affinity mafic rock assemblages in the Luobei-Yilan accretionary complex (Ren, 2017; Dong, 2018) and (2) Late Triassic to Middle Jurassic forearc sedimentary successions in the Heilongjiang Complex (Jing et al., 2022), as well as associated arc magmatic rocks (Dong et al., 2017; Zhu et al., 2017c; Ge et al., 2018; Sun et al., 2018). Additional support can be obtained from the metamorphic evolution data, including the clockwise P-T path of the Heilongjiang Complex (Han, 2018) and metamorphic ages of OIB-MORB-type rocks from metamorphosed sedimentary units in the Luobei region (209–185 Ma) (Jing et al., 2022), which collectively indicate subduction processes during the Early Mesozoic.

The syenogranites in the study area are classified as I-type granites with a high K calc-alkaline affinity and are typically formed in convergent plate margin tectonic settings (Wilson, 1989). These rocks are enriched in light rare earth elements (LREEs) and large ion lithophile elements (LILEs), such as Rb and K, and depleted in heavy rare earth elements (HREEs) and high field strength elements (HFSEs), such as Nb, Ta, and Ti, which exhibit geochemical signatures characteristic of igneous rocks generated in subduction zone environments (McCulloch and Gamble, 1991). In the tectonic discrimination diagrams based on trace elements, all granite samples were within the arc-related magmatic rock field (Figure 12), suggesting a volcanic arc tectonic setting. Considering the regional tectonic background, the Early Jurassic (194 Ma) syenogranite in the northern Zhangguangcai Range formed in an active continental margin setting, which could be closely associated with the westward subduction of the Paleo-Pacific Plate and potentially influenced by the overlapping subduction and closure of the Mudanjiang Ocean, a branch of the Paleo-Pacific. First, the Early Mesozoic magmatic belt in the Lesser Xing'an-Zhangguangcai Range was oriented nearly north-south, parallel to the Heilongjiang Complex, and temporally concentrated in the Early Jurassic (200–180 Ma), displaying geochemical traits indicative of subduction fluid-modified magma sources: (1) medium-to high-K calc-alkaline rocks enriched in LREEs and LILEs but depleted in HREEs and HFSEs, consistent with continental arc environments (Zhao et al., 2018; Ge et al., 2020a; Ge et al., 2020b; Xiao et al., 2023); and (2) mafic rocks (gabbro-amphibolites) showing relatively homogeneous Hf isotopic compositions (εHf = +2.7 to +12.0), suggesting the derivation from partial melting of a depleted mantle wedge metasomatized by slab-derived melts (Yu et al., 2012). The tectonic and geophysical evidence further corroborated the

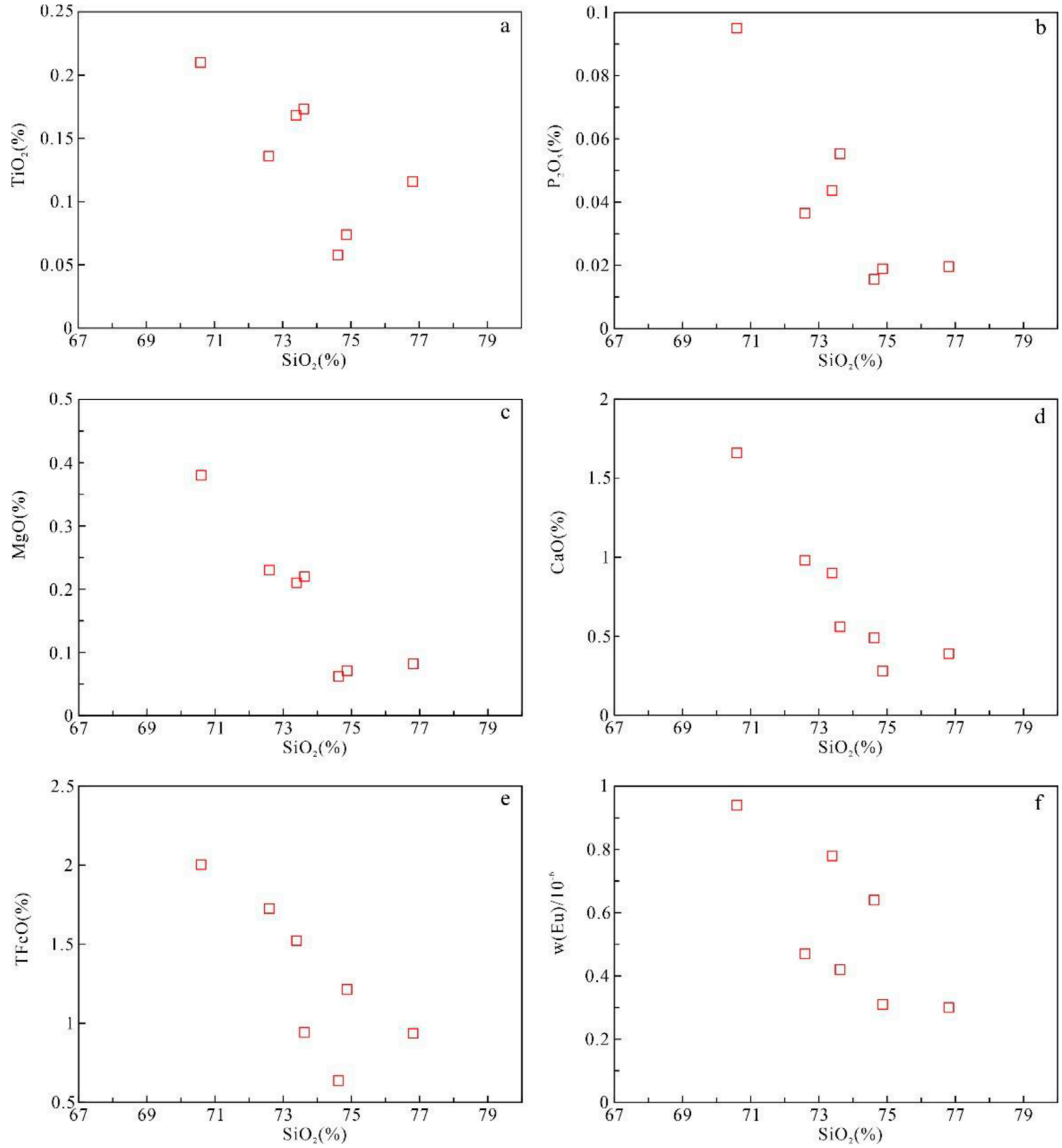

FIGURE 10
Harker variation diagrams for the samples.

subduction setting: (1) the metamorphic age of the Heilongjiang Complex (202–172 Ma) coincided with the formation age of the studied granites, indicating synchronous subduction-related metamorphism and magmatism (Wu et al., 2008; Zhou et al., 2009; Ge et al., 2016; Dong, 2018); (2) geophysical imaging revealed a high-conductivity wedge-shaped anomaly beneath the Songnen Block, interpreted as a relic subducted slab (Liang et al., 2017); and (3) structural evidence, including regional-scale sinistral ductile shear zones and tectonic fabric analysis, suggested an Early Jurassic oblique compression regime (Shao et al., 2013). Additionally, the analysis of the spatial and temporal distribution of granitic rocks in the Lesser Xing'an–Zhangguangcai Range (Figure 8b) revealed a westward younging trend in Early Mesozoic magmatism, potentially linked to progressive flattening of the Paleo-Pacific subduction angle during this period.

6 Conclusion

1. The zircon U-Pb age of the syenogranite in the study area was 194 ± 2 Ma (n = 17, MSWD = 1.15), indicating its emplacement during the Early Jurassic. Combined with the regional chronological data analysis, this suggested that large-scale magmatic activity occurred in the Lesser Xing'an - Zhangguangcai Range during the Early Jurassic.

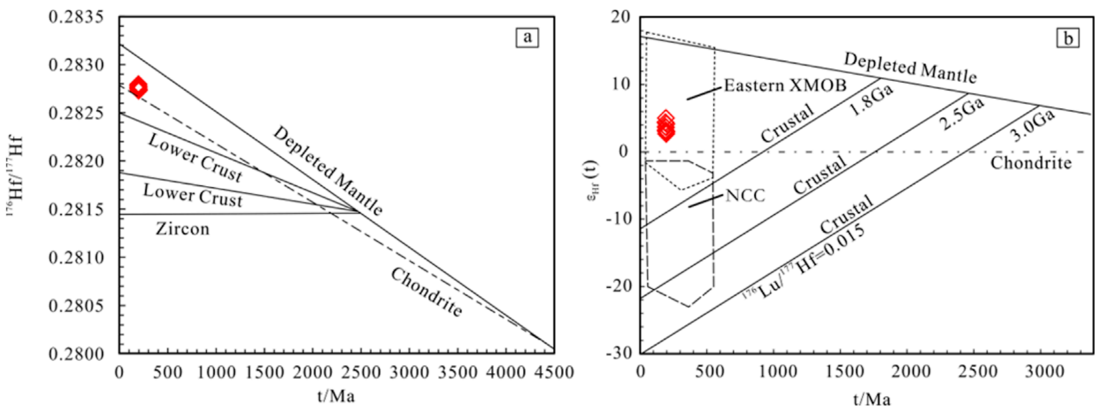

FIGURE 11
The diagrams between Hf isotopic compositions and the U-Pb age of zircons for the syenogranite in the study area. **(a)** ^{176}Hf/^{177}Hf-t diagram (Wu F. et al., 2007); **(b)** ε_{Hf}(t)-t diagram (Yang et al., 2006).

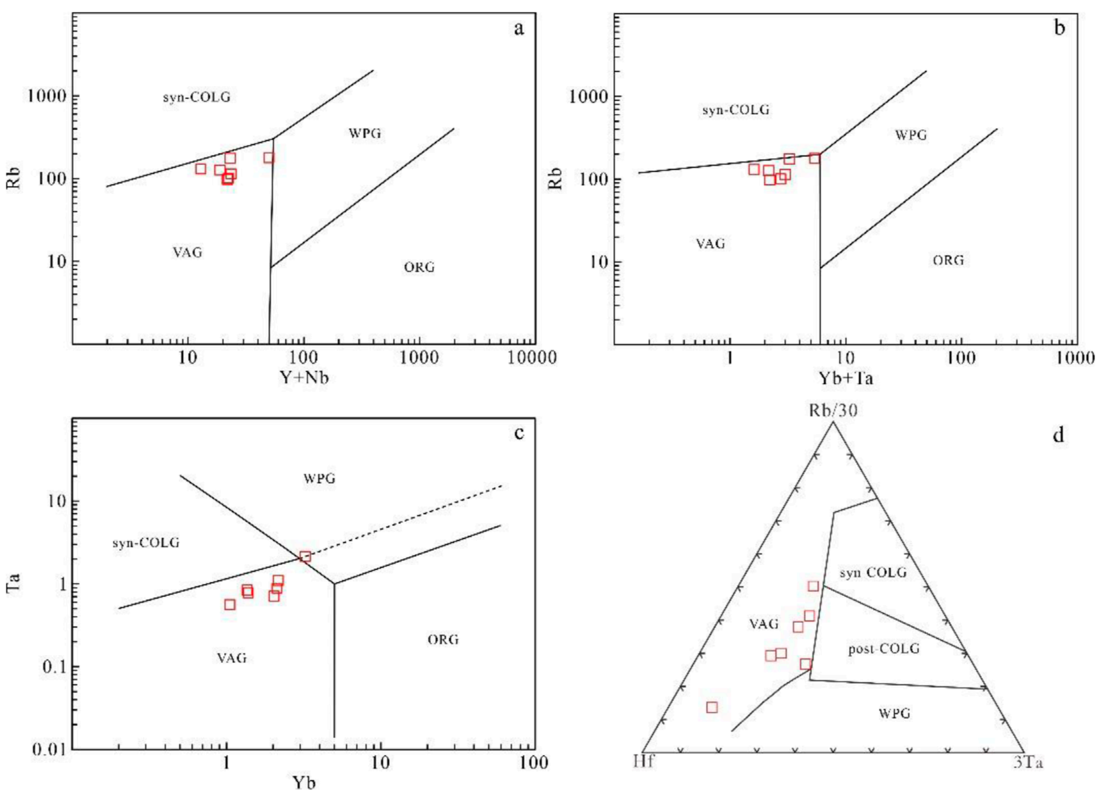

FIGURE 12
Tectonic discrimination diagrams for the syenogranite in the study area (Harris et al., 1986; Pearce, 1996). **(a)** Rb-(Y + Nb) diagram; **(b)** Rb-(Yb + Ta) diagram; **(c)** Ta-Yb diagram; **(d)** Rb/30-Hf-Ta×3 diagram.

2. The syenogranite in the northern section of the Zhangguangcai Range was characterized as quasi-aluminous to weakly peraluminous with a high-potassium calc-alkaline affinity, having undergone significant crystallization differentiation during magma evolution, and was classified as a highly differentiated I-type granite.
3. Based on the analysis of geochemical characteristics and zircon Hf isotopic signatures, the magma of the syenogranite within the study area was primarily derived from the partial melting of juvenile amphibolite-facies basic lower crust formed during the Mesoproterozoic to Neoproterozoic.
4. Based on the regional geology, isotopic geochronology, and petrogeochemical characteristics, the syenogranite intrusions within the study area were formed in an active continental margin environment, closely associated with the westward subduction of the Paleo-Pacific Ocean during the Early

Jurassic, which may have also been influenced by the superimposed subduction-closure process of the Mudanjiang Ocean, a branch of the Paleo-Pacific Ocean.

Data availability statement

The original contributions presented in the study are included in the article/Supplementary Material, further inquiries can be directed to the corresponding authors.

Author contributions

LL: Conceptualization, Formal Analysis, Investigation, Writing – original draft, Writing – review and editing. MD: Writing – review and editing. JH: Funding acquisition, Writing – review and editing. HS: Investigation, Writing – review and editing. XL: Supervision, Writing – review and editing. YZ: Writing – review and editing.

Funding

The author(s) declare that financial support was received for the research and/or publication of this article. This research was funded by the project of Northeast Geological S&T Innovation Center of China Geological Survey (Grants QCJJ2024-17 and QCJJ 2022-2) and China Geological Survey Project (Grants DD20230508, DD20220852 and DD20242940).

Conflict of interest

The authors declare that the research was conducted in the absence of any commercial or financial relationships that could be construed as a potential conflict of interest.

Generative AI statement

The author(s) declare that no Generative AI was used in the creation of this manuscript.

Publisher's note

All claims expressed in this article are solely those of the authors and do not necessarily represent those of their affiliated organizations, or those of the publisher, the editors and the reviewers. Any product that may be evaluated in this article, or claim that may be made by its manufacturer, is not guaranteed or endorsed by the publisher.

Supplementary material

The Supplementary Material for this article can be found online at: https://www.frontiersin.org/articles/10.3389/feart.2025.1578301/full#supplementary-material

References

Amelin, Y., Lee, D. C., and Halliday, A. (2000). Early-Middle Archaean crustal evolution deduced +rom Lu-Hf and U-Pb isotopic studies of single zircon grains. *Geochimica Cosmochimica Acta* 64, 4205–4225. doi:10.1016/S0016-7037(00)00493-2

Amelin, Y., Lee, D. C., Halliday, A. N., and Pidgeon, R. T. (1999). Nature of the Earth's earliest crust from hafnium isotopes in single detrital zircons. *Nature* 399, 252–255. doi:10.1038/20426

Ao, G. (2016). Zircon U-Pb LA-ICP-MS Age of the intrusive rock in southern Zhangguangcailing area. *Geol. Resour.* 25, 533–538. doi:10.13686/j.cnki.dzyzy.2016.06.004

Bao, Z., Wang, J., Yang, Y., Wang, L., Xie, Z., Song, Y., et al. (2014). U-Pb dating and Hf isotopic composition of ore-hosting granites from the pingdingshan gold deposit, Heilongjiang province, and its geological implications. *Acta Geol. Sin.* 88, 407–420. doi:10.19762/j.cnki.dizhixuebao.2014.03.009

Barth, M. G., McDonough, W. F., and Rudnick, R. L. (2000). Tracking the budget of Nb and Ta in the continental crust. *Chem. Geol.* 165, 197–213. doi:10.1016/s0009-2541(99)00173-4

Chappell, B. (1999). Aluminium saturation in I- and S-type granites and the characterization of fractionated haplogranites. *Lithos* 46, 535–551. doi:10.1016/S0024-4937(98)00086-3

Chappell, B. W., and White, A. J. R. (2001). Two contrasting granite types: 25 years later. *Aust. J. Earth Sci.* 48, 489–499. doi:10.1046/j.1440-0952.2001.00882.x

Cheng, G., Wang, R., Zeng, Q., Guo, Y., Duan, X., Wei, J., et al. (2015). Zircon U-Pb ages, Hf isotopes of the granitoids and Re-Os ages of the molybdenites in Luming molybdenum ore area, Heilongjiang Province, and its geological significance. *Acta Petrol. Sin.* 31, 2450–2464.

De La Roche, H., Leterrier, J., Grandclaude, P., and Marchal, M. (1980). A classification of volcanic and plutonic rocks using R 1 R 2 -diagram and major-element analyses — its relationships with current nomenclature. *Chem. Geol.* 29, 183–210. doi:10.1016/0009-2541(80)90020-0

Dong, Y. (2018). *Convergence history of the Jiamusi and songnen-zhangguangcai range massifs geochronological and geochemical evidence.* (PhD thesis). Jilin University, Changchun, China.

Dong, Y., Ge, W., Yang, H., Bi, J., Wang, Z., and Xu, W. (2017). Permian tectonic evolution of the Mudanjiang Ocean: evidence from zircon UPbHf isotopes and geochemistry of a NS trending granitoid belt in the Jiamusi Massif, NE China. *Gondwana Res.* 49, 147–163. doi:10.1016/j.gr.2017.05.017

Dong, Y., Ge, W., Yang, H., Ji, Z., He, Y., Zhao, D., et al. (2018). Convergence history of the Jiamusi and SongnenZhangguangcai range massifs: insights from detrital zircon UPb geochronology of the yilan Heilongjiang complex, NE China. *Gondwana Res.* 56, 51–68. doi:10.1016/j.gr.2017.12.008

Du, B. Y., Liu, F., Liu, Y., Liu, Y. W., Gao, H. Y., Zhen, M., et al. (2022). Permian—early Jurassic ocean—continent evolution and metallogenic dynamic setting in the central and eastern part of Heilongjiang Province. *Geol. Rev.* 68, 431–451. doi:10.16509/j.georeview.2022.01.105

Duan, Z. P., Jiang, S. Y., Su, H. M., Zhu, X. Y., Zou, T., and Cheng, X. Y. (2021). Geochronological and geochemical investigations of the granites from the giant Shihuiyao Rb-(Nb-Ta-Be-Li) deposit, Inner Mongolia: implications for magma source, magmatic evolution, and rare metal mineralization. *Lithos* 400–401, 106415. doi:10.1016/j.lithos.2021.106415

Eby, G. N. (1992). Chemical subdivision of the A-type granitoids: petrogenetic and tectonic implications. *Geology* 20, 641–644. doi:10.1130/0091-7613(1992)020<0641:csotat>2.3.co;2

Fei, X., Zhang, Z., Cheng, Z., Santosh, M., Jin, Z., Wen, B., et al. (2018). Highly differentiated magmas linked with polymetallic mineralization: a case study from the Cuihongshan granitic intrusions, Lesser Xing'an Range, NE China. *Lithos* 302–303, 158–177. doi:10.1016/j.lithos.2017.12.027

Feng, G., Dilek, Y., Niu, X., Liu, F., and Yang, J. (2021). Geochemistry and geochronology of OIB-type, Early Jurassic magmatism in the Zhangguangcai range, NE China, as a result of continental back-arc extension. *Geol. Mag.* 158, 143–157. doi:10.1017/S0016756818000705

Feng, G., Niu, X., Liu, F., Liu, S., and Yang, J. (2019). Petrogenesis of late Early Jurassic granodiorites and associated dioritic enclaves in the Zhangguangcai Range and its tectonic implications. *Acta Geol. Sin.* 93, 2598–2616. doi:10.19762/j.cnki.dizhixuebao.2019258

Ge, M. H., Zhang, J. J., Li, L., and Liu, K. (2018). A TriassicJurassic westward scissorLike subduction history of the Mudanjiang Ocean and amalgamation of the Jiamusi Block in NE China: constraints from wholeRock geochemistry and zircon UPb and LuHf isotopes of the Lesser Xing'an-Zhangguangcai Range granitoids. *Lithos* 302, 263–277. doi:10.1016/j.lithos.2018.01.004

Ge, M. H., Zhang, J. J., Li, L., and Liu, K. (2019). Ages and geochemistry of early jurassic granitoids in the lesser xing'an–zhangguangcai ranges, NE China: petrogenesis and tectonic implications. *Lithosphere* 11, 804–820. doi:10.1130/L1099.1

Ge, M. H., Zhang, J. J., Li, L., Liu, K., Ling, Y. Y., Wang, J. M., et al. (2017). Geochronology and geochemistry of the Heilongjiang complex and the granitoids from the lesser xing'an-zhangguangcai range: implications for the late PaleozoicMesozoic tectonics of eastern NE China. *Tectonophysics* 717, 565–584. doi:10.1016/j.tecto.2017.09.004

Ge, M. H., Zhang, J. J., and Liu, K. (2020a). Geochronology, geochemistry and zircon Hf isotope of the Jurassic diabase from the Tieli area, Lesser Xing'an-Zhangguangcai Range, and its geological implications. *Acta Petrol. Sin.* 36, 726–740. doi:10.18654/1000-0569/2020.03.06

Ge, M. H., Zhang, J. J., Liu, K., Ling, Y. Y., Wang, M., and Wang, J. M. (2016). Geochemistry and geochronology of the blueschist in the Heilongjiang Complex and its implications in the late Paleozoic tectonics of eastern NE China. *Lithos* 261, 232–249. doi:10.1016/j.lithos.2015.11.019

Ge, M. H., Zhang, J. J., Liu, K., Wang, M., and Li, Z. (2020b). Petrogenesis of the late paleozoic to mesozoic granite from the Xiao hinggan mountains-zhangguangcai mountains and its geological implications. *Acta Petrol. Mineral.* 39, 385–405.

Geng, W. (2015). *Petrogenesis and their geological significance of the granites from Shangzhi area, southern section of Zhangguangcai Range*. (master's thesis). North West University, Xi'an, China.

Gong, H. J., Zhu, L. M., Sun, B. Y., Li, B., Guo, B., and Wang, J. Q. (2009). Zircon U-Pb ages and Hf isotopic composition of the Dongjiangkou granitic pluton and its mafic enclaves in the South Qinling terrain. Acta Petrol. *Sin.* 25, 3029–3042.

Green, T. (1995). Significance of Nb/Ta as an indicator of geochemical processes in the crust-mantle system. *Chem. Geol.* 120, 347–359. doi:10.1016/0009-2541(94)00145X

Guo, P., Xu, W. L., Wang, Z. W., Wang, F., and Luan, J. P. (2018). Geochronology and geochemistry of late DevonianCarboniferous igneous rocks in the SongnenZhangguangcai range massif, NE China: constraints on the late paleozoic tectonic evolution of the eastern central asian orogenic belt. *Gondwana Res.* 57, 119–132. doi:10.1016/j.gr.2018.01.007

Han, X. (2018). *Blueschist facies metamorphism in Northeastern China*. (PhD thesis). Jilin University, Changchun, China.

Han, Z. Z., Ren, X., Schertl, H. P., Li, X. P., Song, Z. G., Du, Q. X., et al. (2020). Zircon U-Pb-Hf isotopes and geochemistry of Jurassic igneous rocks from the southern Zhangguangcai Range, NE China: constraints on magmatism, petrogenesis and tectonic implications. *Int. Geol. Rev.* 62, 1988–2012. doi:10.1080/00206814.2019.1681302

Harris, N. B. W., Pearce, J. A., and Tindle, A. G. (1986). Geochemical characteristics of collisionZone magmatism. *Geol. Soc. Lond. Spec. Publ.* 19, 67–81. doi:10.1144/gsl.sp.1986.019.01.04

Heilongjiang Bureau of Geology and Mineral Resources (1993). *Regional geology of Heilongjiang province*. Beijing: Geological Publishing House.

Hou, K. (2009). *In situ* U-Pb zircon dating using laser ablation Multi ion counting ICP-MS. *Mineral. Deposits* 28, 481–492. doi:10.3969/j.issn.0258-7106.2009.04.010

Hu, X., Ding, Z., He, M., Yao, S., Zhu, B., Shen, J., et al. (2014). A porphyry-skarn metallogenic system in the Lesser Xing'an Range, NE China: implications from U–Pb and Re–Os geochronology and Sr–Nd–Hf isotopes of the Luming Mo and Xulaojiugou Pb–Zn deposits. *J. Asian Earth Sci.* 90, 88–100. doi:10.1016/j.jseaes.2014.04.020

Jahn, B., Windley, B., Natal'in, B., and Dobretsov, N. (2004). Phanerozoic continental growth in central asia. *J. Asian Earth Sci.* 23, 599–603. doi:10.1016/S1367-9120(03)00124-X

Ji, Z., Zhang, Y., Wan, C., Ge, W., Yang, H., Dong, Y., et al. (2021). Recycling of crustal materials and implications for lithospheric thinning: evidence from Mesozoic volcanic rocks in the Hailar–Tamtsag Basin, NE China. *Geosci. Front.* 12, 101184. doi:10.1016/j.gsf.2021.101184

Jilin Bureau of Geology and Mineral Resources (1988). *Regional geology of Jilin province*. Beijing: Geological Publishing House.

Jing, J., Yang, H., Ge, W., Ji, Z., Zhang, Y., Dong, Y., et al. (2022). Provenance and metamorphic records of forearc sediments from the Heilongjiang Complex, NE China: implications for subduction erosion associated with the Mudanjiang Ocean. *GSA Bull.* 134, 3049–3063. doi:10.1130/B36218.1

Klein, M., Stosch, H. G., and Seck, H. A. (1997). Partitioning of high field-strength and rare-earth elements between amphibole and quartz-dioritic to tonalitic melts: an experimental study. *Chem. Geol.* 138, 257–271. doi:10.1016/S0009-2541(97)00019-3

Kong, J., Qiao, K., Huo, X., Zhang, G., Chen, X., and Yao, L. (2024). Geochronology and geochemical characteristics of granitoids in the lesser xing'an–zhangguangcai range: petrogenesis and implications for the early jurassic tectonic evolution of the Mudanjiang Ocean. *Minerals* 14, 941. doi:10.3390/min14090941

Li, B. L., Sun, Y. G., Chen, G. J., Xi, A. H., Zhi, Y. B., Chang, J. J., et al. (2016). Zircon U-Pb geochronology, geochemistry and Hf isotopic composition and its geological implication of the fine-grained syenogranite in Dong'an goldfield from the lesser Xing'an Mountains. *Earth Sci.* 41, 1–16. doi:10.3799/dqkx.2016.001

Li, H., Han, J., Zhao, Z., and Yin, Z. (2023). Magma-mixing origin for the early jurassic intrusive rocks in the eastern songnen–zhangguangcai range massif, NE China: evidence from geochronology, geochemistry and Hf–O–Sr–Nd isotopes. *Gondwana Res.* 121, 72–91. doi:10.1016/j.gr.2023.04.002

Li, R. (2013). *Age, geochemistry and petrogenesis of the Weihe granite batholith in the northern Zhangguangcai Range*. (master's thesis). Jilin University, Jilin, China.

Li, X. H., Li, Z. X., Li, W. X., Liu, Y., Yuan, C., Wei, G., et al. (2007). U–Pb zircon, geochemical and Sr–Nd–Hf isotopic constraints on age and origin of Jurassic I- and A-type granites from central Guangdong, SE China: a major igneous event in response to foundering of a subducted flat-slab? *Lithos* 96, 186–204. doi:10.1016/j.lithos.2006.09.018

Liang, H., Jin, S., Wei, W., Gao, R., Hou, H., Han, J., et al. (2017). Deep electrical structures of the eastern margin of the Songnen massif and the western margin of the Jiamusi massif. *Acta geophys.* 60, 1511–1520. doi:10.6038/cjg20170423

Liu, C., Wu, C., Gao, Y., Lei, M., Qin, H., and Li (2014). Zircon LA-ICP-MS U-Pb dating and Lu-Hf isotopic system of A-type granitoids in south tianshan, baicheng county, xinjiang. *Acta Petrol. Sin.* 30, 1595–1614.

Liu, J., Chi, X., Dong, C., Zhao, Z., Li, G., and Zhao, Y. (2008). Discovery of early Paleozoic granites in the eastern Xiao Hinggan Mountains, northeastern China and their tectonic significance. *Geol. Bull. China* 27, 534–544.

Liu, K., Zhang, J., Wilde, S. A., Zhou, J., Wang, M., Ge, M., et al. (2017). Initial subduction of the PaleoPacific Oceanic plate in NE China: constraints from wholeRock geochemistry and zircon U–Pb and Lu–Hf isotopes of the Khanka Lake granitoids. *Lithos* 274, 254–270. doi:10.1016/j.lithos.2016.12.022

Liu, K., Zhang, J. J., Ge, M. H., and Ling, Y. Y. (2016). Mesozoic subduction of the Paleo-Pacific Plate along the eastern margin of the xing-meng orogenic belt. *Bull. Mineral. Petrol. Geochem.* 35, 1098–1108.

Long, X. Y., Xu, W. L., Guo, P., Sun, C. Y., and Luan, J. P. (2020a). Opening and closure history of the Mudanjiang Ocean in the eastern central asian orogenic belt: geochronological and geochemical constraints from early mesozoic intrusive rocks. *Gondwana Res.* 84, 111–130. doi:10.1016/j.gr.2020.03.003

Long, X. Y., Xu, W. L., Guo, P., Sun, C. Y., and Luan, J. P. (2020b). Was Permian magmatism in the eastern Songnen and western Jiamusi massifs, NE China, related to the subduction of the Mudanjiang oceanic plate? *Geol. J.* 55, 1781–1807. doi:10.1002/gj.3577

Maniar, P. D., and Piccoli, P. M. (1989). Tectonic discrimination of granitoids. *Geol. Soc. Am. Bull.* 101, 635–643. doi:10.1130/0016-7606(1989)101<0635:tdog>2.3.co;2

McCulloch, M. T., and Gamble, J. A. (1991). Geochemical and geodynamical constraints on subduction zone magmatism. *Earth Planet. Sci. Lett.* 102, 358–374. doi:10.1016/0012-821X(91)90029H

Middlemost, E. A. (1994). Naming materials in the magma/igneous rock system. *Earth-Sci. Rev.* 37, 215–224. doi:10.1016/0012-8252(94)90029-9

Norris, A., and Danyushevsky, L. (2018). *Towards estimating the complete uncertainty budget of quantified results measured by LAICPMS*. Boston, MA, USA: Goldschmidt.

Ouyang, H., Caulfield, J., Mao, J., and Hu, R. (2022). Controls on the formation of porphyry Mo deposits: insights from porphyry (-skarn) Mo deposits in northeastern China. *Am. Mineral.* 107, 1736–1751. doi:10.2138/am-2021-7665

Pearce, J. (1996). Sources and settings of granitic rocks. *Episodes* 19, 120–125. doi:10.18814/epiiugs/1996/v19i4/005

Qian, Q., Chung, S. L., Lee, T. Y., and Wen, D. R. (2002). Geochemical characteristics and petrogenesis of the Badaling high BaSr granitoids: a comparison of igneous rocks from North China and the DabieSulu Orogen. *Acta Petrol. Sin.* 18, 275–292. doi:10.3969/j.issn.1000-0569.2002.03.002

Qian, Q., and Hermann, J. (2013). Partial melting of lower crust at 10–15 kbar: constraints on adakite and TTG formation. *Contrib. Mineral. Petrol.* 165, 1195–1224. doi:10.1007/s00410-013-0854-9

Qin, J. F., Lai, S. C., Li, Y. F., Ju, Y. J., Zhu, R. Z., and Zhao, S. W. (2016). Early Jurassic monzograniteTonalite association from the southern Zhangguangcai Range: implications for paleo–Pacific plate subduction along northeastern China. *Lithosphere* 8, 396–411. doi:10.1130/L505.1

Qiu, J., Xiao, E., Hu, J., Xu, X., Jiang, S., and Li, Z. (2008). Petrogenesis of highly fractionated IType granites in the coastal area of northeastern Fujian Province: constraints from zircon UPb geochronology, geochemistry and NdHf isotopes. *Acta Petrol. Sin.* 24, 2468–2484. Available online at: https://academic.microsoft.com/paper/2365269587.

Qiu, K. F., Zhou, T., Chew, D., Hou, Z. L., Muller, A., Yu, H. C., et al. (2024). Apatite trace element composition as an indicator of ore deposit types: a machine learning approach. *Am. Min.* 109, 303–314. doi:10.2138/am-2022-8805

Quan, J., Chi, X., Zhang, R., Sun, W., Fan, L., and Hu, Z. (2013). LA–ICP–MS U–Pb geochronology of detrital zircon from the Neoproterozoic Dongfengshan Group in Songnen masiff and its geological significance. *Geol. Bull. China* 32, 353–364. doi:10.3969/j.issn.1671-2552.2013.02.014

Rapp, R. P., and Watson, E. B. (1995). Dehydration melting of metabasalt at 8-32 kbar: implications for continental growth and crust-mantle recycling. *J. Petrol.* 36, 891–931. doi:10.1093/petrology/36.4.891

Ren, Y. (2019). Early-Middle Jurassic granitic magmatism and tectonic evolution in the southern part of Zhangguangcailing. *Acta Geol. Sin.* 93, 2813–2831. doi:10.19762/j.cnki.dizhixuebao.2019199

Ren, Z. (2017). *Petrogenesis and tectonic implications of the Northern Luobei amphibolite and metagabbro from the western margin of the Jiamusi Massif.* (master's thesis). Jilin University, Changchun, China.

Rollinson, H. R. (1993). *Using geochemical data: evaluation, presentation, interpretation*. London: Longman Scientific and Technical.

Rubatto, D. (2002). Zircon trace element geochemistry: partitioning with garnet and the link between U–Pb ages and metamorphism. *Chem. Geol.* 184, 123–138. doi:10.1016/S0009-2541(01)00355-2

Rudnick, R., and Gao, S. (2003). The role of lower crustal recycling in continent formation. *Geochim. Cosmochim. Acta* 67, A403.

Şengör, A., Natal'In, B., and Burtman, V. (1993). Evolution of the Altaid tectonic collage and Palaeozoic crustal growth in Eurasia. *Nature* 364, 299–307. doi:10.1038/364299a0

Sha, L. K., and Chappell, B. W. (1999). Apatite chemical composition, determined by electron microprobe and laserAblation inductively coupled plasma mass spectrometry, as a probe into granite petrogenesis. *Geochim. Cosmochim. Acta* 63, 3861–3881. doi:10.1016/S0016-7037(99)00210-0

Shao, J., Li, Y., and Tang, K. (2013). Restoration of the orogenic processes of Zhangguangcai range. *Acta Petrol. Sin.* 29, 2959–2970.

Sláma, J., Košler, J., Condon, D. J., Crowley, J. L., Gerdes, A., Hanchar, J. M., et al. (2008). Plešovice zircon—a new natural reference material for U–Pb and Hf isotopic microanalysis. *Chem. Geol.* 249, 1–35. doi:10.1016/j.chemgeo.2007.11.005

Soesoo, A. (2000). Fractional crystallization of mantle-derived melts as a mechanism for some I-type granite petrogenesis: an example from Lachlan Fold Belt, Australia. *J. Geol. Soc.* 157, 135–149. doi:10.1144/jgs.157.1.135

Streckeisen, A. L. (1973). Plutonic rock: classification and nomenclature recommended by the IUGS subcommission on the systematics of igneous rocks. *Geotimes* 18, 26–30.

Sun, D., Wu, F., and Gao, S. (2004). LA-ICP-MS zircon U-Pb age of the qingshui pluton in the east Xiao hinggan mountains. *Acta Geosci. Sin.* 25, 213–218. doi:10.3321/j.issn:1006-3021

Sun, M., Chen, H., Milan, L. A., Wilde, S. A., Jourdan, F., and Xu, Y. (2018). Continental Arc and back-arc migration in eastern NE China: new constraints on cretaceous paleo-pacific subduction and rollback. *Tectonics* 37, 3893–3915. doi:10.1029/2018TC005170

Sun, M., Xu, Y., Wilde, S. A., Chen, H., and Yang, S. (2015). The permian dongfanghong island-arc gabbro of the wandashan orogen, NE China: implications for paleo-pacific subduction. *Tectonophysics* 659, 122–136. doi:10.1016/j.tecto.2015.07.034

Sun, S. S., and McDonough, W. F. (1989). Chemical and isotopic systematics of oceanic basalts: implications for mantle composition and processes. *Geol. Soc. Lond. Spec. Publ.* 42, 313–345. doi:10.1144/GSL.SP.1989.042.01.19

Sun, X. (2016). *On study of chronology and tectonic environment of the Jurassic granites in the south of Zhangguangcai Range*. Changchun China: Jilin University.

Sylvester, P. J. (1989). Post-collisional alkaline granites. *J. Geol.* 97, 261–280. doi:10.1086/629302

Tan, H., Shu, G., Lu, J., Han, R., Zhang, S., and Kou, L. (2012). LA-ICP-MS zircon uranium-lead and molybdenite rhenium-osmium dating for the Luming large-scale molybdenum deposit in Xiao Hinggan Mountains and its geological implication. *Jilin Daxue Xuebao Diqiu Kexue Ban/Journal Jilin Univ. Earth Sci. Ed.* 42, 1757–1770. doi:10.13278/j.cnki.jjuese.2012.06.001

Tan, H., Wang, D., Lv, J., Shu, G., and Han, R. (2013). Petrogenesis and mineralization chronology study on the Huojihe molybdenum deposit Xiao Hinggan Mountains and its geological implication. *Acta Petrol. Miner.* 32, 733–750. doi:10.3969/j.issn.1000-6524.2013.05.013

Tang, J., Xu, W., Wang, F., and Ge, W. (2018). Subduction history of the PaleoPacific slab beneath eurasian continent: MesozoicPaleogene magmatic records in Northeast asia. *Sci. China Earth Sci.* 61, 527–559. doi:10.1007/s11430-017-9174-1

Taylor, S. R., and Mclennan, S. M. (1985). *The continental crust: its composition and evolution*. Amsterdam, Netherlands: Blackwell Scientific Publications.

Vervoort, J. D., Patchett, P., Gehrels, G., and Nutman, A. (1996). Constraints on early Earth differentiation from hafnium and neodymium isotopes. *Nature* 379, 624–627. doi:10.1038/379624a0

Wang, F., Xu, W. L., Gao, F. H., Zhang, H. H., Pei, F. P., Zhao, L., et al. (2014). Precambrian terrane within the songnen–zhangguangcai range massif, NE China: evidence from U–Pb ages of detrital zircons from the dongfengshan and tadong groups. *Gondwana Res.* 26, 402–413. doi:10.1016/j.gr.2013.06.017

Wang, F., Xu, W. L., Meng, E., Cao, H. H., and Gao, F. H. (2012). Early paleozoic amalgamation of the songnen–zhangguangcai range and Jiamusi massifs in the eastern segment of the central asian orogenic belt: geochronological and geochemical evidence from granitoids and rhyolites. *J. Asian Earth Sci.* 49, 234–248. doi:10.1016/j.jseaes.2011.09.022

Wang, F., Xu, W. L., Xu, Y. G., Gao, F., and Ge, W. (2015). Late triassic bimodal igneous rocks in eastern Heilongjiang province, NE China: implications for the initiation of subduction of the Paleo-Pacific Plate beneath eurasia. *J. Asian Earth Sci.* 97, 406–423. doi:10.1016/j.jseaes.2014.05.025

Wang, F., Xu, Y. G., Xu, W. L., Yang, L., Wu, W., and Sun, C. Y. (2017a). Early Jurassic calcAlkaline magmatism in northeast China: magmatic response to subduction of the PaleoPacific Plate beneath the Eurasian continent. *J. Asian Earth Sci.* 143, 249–268. doi:10.1016/j.jseaes.2017.04.018

Wang, N., Zhang, Z., Malusà, M. G., Wu, L., Chew, D., Zhang, J., et al. (2021). Pulsed Mesozoic exhumation in Northeast Asia: new constraints from zircon U-Pb and apatite U-Pb, fission track and (U-Th)/He analyses in the Zhangguangcai Range, NE China. *Tectonophysics* 818, 229075. doi:10.1016/j.tecto.2021.229075

Wang, S., Liu, J., Ji, H., Lv, J., Zhou, S., and Liu, J. (2017c). Geochronology and geochemistry of the andesites of longjiang formation in the sandaowanzi gold deposit, Heilongjiang province. *Acta Petrol. Sin.* 33, 2604–2618.

Wang, W., Chen, G., Wang, C., Zhu, R., Chen, J., Ren, L., et al. (2022). Early Jurassic granodiorite-monzogranite-granite suite in the Zhangguangcai Range, NE China: implications for melting of newly accreted arc crust. *Geol. J.* 57, 1110–1124. doi:10.1002/gj.4324

Wang, Z. (2016). *Late Paleozoic-Triassic tectonic evolution of eastern segment of the southern margin of the Xing'an-Mongolia Orogenic Belt: evidence from detrital zircon U-Pb geochronology and igneous rock associations*. (dissertation's thesis). Jilin University, Changchun, China.

Wang, Z. H., Ge, W. C., Yang, H., Bi, J. H., Ji, Z., Dong, Y., et al. (2017b). Petrogenesis and tectonic implications of Early Jurassic volcanic rocks of the Raohe accretionary complex, NE China. *J. Asian Earth Sci.* 134, 262–280. doi:10.1016/j.jseaes.2016.09.021

Wang, Z. Z., Liu, D., Zhao, Z. D., Yan, J. J., Shi, Q. S., and Mo, X. X. (2017d). The Sangri highly fractionated I-type granites in southern Gangdese: petrogenesis and dynamic implication. *Acta Petrol. Sin.* 33, 2479–2493.

Watson, E. B., and Harrison, T. M. (1983). Zircon saturation revisited: temperature and composition effects in a variety of crustal magma types. *Earth Planet. Sci. Lett.* 64, 295–304. doi:10.1016/0012-821X(83)90211X

Whalen, J. B., Currie, K. L., and Chappell, B. W. (1987). AType granites: geochemical characteristics, discrimination and petrogenesis. *Contrib. Mineral. Petrol.* 95, 407–419. doi:10.1007/BF00402202

Wilson, M. (1989). "Active continental margins," in *Igneous petrogenesis* (Dordrecht: Springer Netherlands), 191–225.

Wu, F., Jahn, B., Wilde, S., and Sun, D. (2000). Phanerozoic crustal growth: U–Pb and Sr–Nd isotopic evidence from the granites in northeastern China. *Tectonophysics* 328, 89–113. doi:10.1016/S0040-1951(00)00179-7

Wu, F., Jahn, B., Wilde, S. A., Lo, C. H., Yui, T. F., Lin, Q., et al. (2003a). Highly fractionated I-type granites in NE China (I): geochronology and petrogenesis. *Lithos* 66, 241–273. doi:10.1016/S0024-4937(02)00222-0

Wu, F., Jahn, B., Wilde, S. A., Lo, C. H., Yui, T. F., Lin, Q., et al. (2003b). Highly fractionated I-type granites in NE China (II): isotopic geochemistry and implications for crustal growth in the Phanerozoic. *Lithos* 67, 191–204. doi:10.1016/S0024-4937(03)00015-X

Wu, F., Li, X., Zheng, Y., Gao, S., and others (2007a). Lu-Hf isotopic systematics and their applications in petrology.

Wu, F., Sun, D., Li, H., Jahn, B., and Wilde, S. (2002). A-type granites in northeastern China: age and geochemical constraints on their petrogenesis. *Chem. Geol.* 187, 143–173. doi:10.1016/S0009-2541(02)00018-9

Wu, F., Yang, J., Wilde, S. A., Sun, D., and Jahn, B. (2008). The Heilongjiang group: a Jurassic accretionary complex in the Jiamusi Massif at the western Pacific margin of northeastern China. *Isl. Arc* 16, 156–172. doi:10.1111/j.1440-1738.2007.00564.x

Wu, F. Y., Sun, D. Y., Ge, W. C., Zhang, Y. B., Grant, M. L., Wilde, S. A., et al. (2011). Geochronology of the Phanerozoic granitoids in northeastern China. *J. Asian Earth Sci.* 41, 1–30. doi:10.1016/j.jseaes.2010.11.014

Wu, F. Y., Zhao, G. C., Sun, D. Y., Wilde, S. A., and Yang, J. H. (2007b). The hulan group: its role in the evolution of the central asian orogenic belt of NE China. *J. Asian Earth Sci.* 30, 542–556. doi:10.1016/j.jseaes.2007.01.003

Wu, Y., and Zheng, Y. (2004). 锆石成因矿物学研究及其对U-Pb年龄解释的制约. *Chin. Sci. Bull.* 49, 1589–1604. doi:10.1360/csb2004-49-16-1589

Xia, R., Wang, C., Qing, M., Li, W., Carranza, E. J. M., Guo, X., et al. (2015). Zircon U–Pb dating, geochemistry and Sr–Nd–Pb–Hf–O isotopes for the Nan'getan granodiorites and mafic microgranular enclaves in the East Kunlun Orogen: record of closure of the Paleo-Tethys. *Lithos* 234–235, 47–60. doi:10.1016/j.lithos.2015.07.018

Xiao, B., Xiong, L., Zhao, Z., Fu, X., Zhao, Z., Hou, H., et al. (2023). Late Ordovician-Early Silurian extension of the northern margin of the Upper Yangtze Platform (South China) and its impact on organic matter accumulation. *J. Pet. Sci. Eng.* 220, 111238. doi:10.1016/j.petrol.2022.111238

Xu, M. J., Xu, W. L., Wang, F., Gao, F. H., and Yu, J. J. (2013a). Geochronology and geochemistry of the early jurassic granitoids in the central lesser xing' an range, NE China and its tectonic implications. *Acta Petrol. Sin.* 29, 354–368.

Xu, W., Pei, F., Wang, F., Meng, E., Ji, W., Yang, D., et al. (2013c). Spatial Temporal relationships of Mesozoic volcanic rocks in NE China: constraints on tectonic overprinting and transformations between multiple tectonic regimes. *J. Asian Earth Sci.* 74, 167–193. doi:10.1016/j.jseaes.2013.04.003

Xu, W., Sun, C., Tang, J., Luan, J., and Wang, F. (2019). Basement nature and tectonic evolution of the Xing'anMongolian orogenic belt. *Earth Sci.* 44, 1620–1646. doi:10.3799/dqkx.2019.036

Xu, W., Wang, F., Pei, F., Meng, E., Tang, J., Xu, M., et al. (2013b). Mesozoic tectonic regimes and regional ore-forming background in NE China: constraints from spatial and temporal variations of Mesozoic volcanic rock associations. *Acta Petrol. Sin.* 29, 339–353.

Xu, W. L., Ji, W. Q., Pei, F. P., Meng, E., Yu, Y., Yang, D. B., et al. (2009). Triassic volcanism in eastern Heilongjiang and Jilin provinces, NE China: chronology, geochemistry, and tectonic implications. *J. Asian Earth Sci.* 34, 392–402. doi:10.1016/j.jseaes.2008.07.001

Xue, Y., Tang, J., Xu, W., Luan, J., Long, X., and Liu, H. (2024). Geochronology and geochemistry of early Paleozoic–early Mesozoic magmatic rocks from the Zhangguangcai Range, NE China: constraints on the tectonic evolution of the eastern Songnen Massif. *Geol. J.* 59, 659–679. doi:10.1002/gj.4886

Yang, C., and Wang, Y. (2010). LA-ICPMS zircon U–Pb age and the geological significance for yichun mesozoic granites in southeast lesser khingan range. *Jilin Geol.* 1-5, 31.

Yang, H., Ge, W., Dong, Y., Bi, J., Ji, Z., He, Y., et al. (2019). Permian subduction of the paleo-pacific (panthalassic) oceanic lithosphere beneath the Jiamusi block: geochronological and geochemical evidence from the Luobei mafic intrusions in Northeast China. *Lithos* 332–333, 207–225. doi:10.1016/j.lithos.2019.03.004

Yang, H., Ge, W., Ji, Z., Jing, J., Dong, Y., and Jing, Y. (2022). Phanerozoic magmatism and ocean-continent framework of northeastern China and their relationship with climate change. *Acta Petrol. Sin.* 38, 1443–1459. doi:10.18654/1000-0569/2022.05.11

Yang, H., Ge, W., Zhao, G., Dong, Y., Xu, W., Ji, Z., et al. (2015). Late Triassic intrusive complex in the Jidong region, Jiamusi–Khanka Block, NE China: geochemistry, zircon U–Pb ages, Lu–Hf isotopes, and implications for magma mingling and mixing. *Lithos* 224–225, 143–159. doi:10.1016/j.lithos.2015.03.001

Yang, J. H., Wu, F. Y., Shao, J. A., Wilde, S. A., Xie, L. W., and Liu, X. M. (2006). Constraints on the timing of uplift of the yanshan fold and thrust belt, north China. *Earth Planet. Sci. Lett.* 246, 336–352. doi:10.1016/j.epsl.2006.04.029

Ye, X., Sun, L., Xu, Z., Yan, D., Feng, J., and Cao, R. (2023). Zircon U- Pb geochronology. *Geochem. Charact. Geodyn. Significance Early Jurass. Syenogranite Kaoshan Area Central Jilin Prov. J. Jilin Univ. (Earth Sci. Ed.)* 53, 964–983. doi:10.13278/j.cnki.jjuese.20210147

Ye, X., Sun, L., Xu, Z., Yan, D., Yang, Q., Zhu, D., et al. (2022). Geochemistry and zircon U–PB dating of EARLY JURASSIC syenogranite in the Kaoshan area, southern part of the Zhangguangcai Range, NE China, and tectonic implications. *Geol. J.* 57, 440–461. doi:10.1002/gj.4308

Yin, Z., Gong, Z., Wang, C., Liu, S., Zhang, S., Wang, G., et al. (2021). Chronological, geochemical characteristics and geological significance of early jurassic granites in pingdingshan area of lesser xing'an range. *J. Jilin Univ. (Earth Sci. Ed.)* 51, 107–125. doi:10.13278/j.cnki.jjuese.20190260

Yu, G. Y., Yang, H., Jing, J. H., Ding, X., Ji, Z., Zhang, Y. L., et al. (2023). Tectonic nature, subduction, and closure of the Mudanjiang Ocean: insights from newly discovered oceanic fragments in the Luobei Heilongjiang Complex. *Lithos* 446-447, 107141–107447. doi:10.13278/j.cnki.jjuese.20210147

Yu, J., Wang, F., Xu, W., Gao, F., and Tang, J. (2013). Late Permian tectonic evolution at the southeastern margin of the Songnen–Zhangguangcai Range Massif, NE China: constraints from geochronology and geochemistry of granitoids. *Gondwana Res.* 24, 635–647. doi:10.1016/j.gr.2012.11.015

Yu, J. J., Wang, F., Xu, W. L., Gao, F. H., and Pei, F. P. (2012). Early Jurassic mafic magmatism in the Lesser Xing'an–Zhangguangcai Range, NE China, and its tectonic implications: constraints from zircon U–Pb chronology and geochemistry. *Lithos* 142–143, 256–266. doi:10.1016/j.lithos.2012.03.016

Zhang, G., Chen, X., Zhao, Y., Tang, J., Li, R., Feng, Y., et al. (2022). Geochronology, geochemistry and geological significance of the Middle jurassic porphyritic monzogranite in the southern Zhangguangcai range, Heilongjiang province. *Earth Sci. Ed.* 52, 1907–1925. doi:10.13278/j.cnki.jjuese.20210173

Zhang, L. S., Sun, F. Y., Li, B. H., Qian, Y., Zhang, Y. J., Wang, L., et al. (2021). Petrogenesis and tectonic setting of granitoids in the Fu'anpu molybdenum deposit Lesser Xing'an-Zhangguangcai range metallogenic belt: constraints from element geochemistry, zircon U-Pb geochronology and Sr-Nd-Hf isotopes. *Acta Geol. Sin.* 95, 2471–2492. doi:10.19762/j.cnki.dizhixuebao.2021257

Zhang, Y. B., Wu, F. Y., Wilde, S. A., Zhai, M. G., Lu, X. P., and Sun, D. Y. (2004). Zircon U–Pb ages and tectonic implications of 'early paleozoic' granitoids at yanbian, Jilin province, northeast China. *Isl. Arc* 13, 484–505. doi:10.1111/j.1440-1738.2004.00442.x

Zhao, L., Guo, F., Fan, W., and Huang, M. (2018). Roles of subducted pelagic and terrigenous sediments in early jurassic mafic magmatism in NE China: constraints on the architecture of paleo-pacific subduction zone. *JGR Solid Earth* 124, 2525–2550. doi:10.1029/2018JB016487

Zhao, Z., Li, Z., Li, H., Cheng, B., and Yin, Y. (2024). Geochronology, geochemistry, and geological significance of early Jurassic intrusive rocks in the Lesser Xing'an- Zhangguangcai Range, northeast China. *PLoS ONE* 19, e0306465. doi:10.1371/journal.pone.0306465

Zheng, B. (2016). *Age, geochemistry and geological significance of late triassic-early jurassic intrusive rocks in the southeast region of tieli city, Heilongjiang province*. (master's thesis). Jilin University, Changchun, China.

Zhou, J., Wilde, S. A., Zhang, X., Zhao, G., Zheng, C., Wang, Y., et al. (2009). The onset of Pacific margin accretion in NE China: evidence from the Heilongjiang high-pressure metamorphic belt. *Tectonophysics* 478, 230–246. doi:10.1016/j.tecto.2009.08.009

Zhou, Y., Zhao, T., Sun, Q., and Zhai, M. (2018). Geochronological and geochemical constraints on the petrogenesis of the 2.6–2.5 Ga amphibolites, low- and high-Al TTGs in the Wangwushan area, southern North China Craton: implications for the Neoarchean crustal evolution. *Precambrian Res.* 307, 93–114. doi:10.1016/j.precamres.2018.01.013

Zhu, C. Y., Zhao, G., Ji, J., Sun, M., Han, Y., Liu, Q., et al. (2017a). Subduction between the Jiamusi and Songliao blocks: geological, geochronological and geochemical constraints from the Heilongjiang complex. *Lithos* 282–283, 128–144. doi:10.1016/j.lithos.2017.03.008

Zhu, Y., Yang, H., Dong, Y., He, Y., Bi, J., Wang, Z., et al. (2017b). Geochronology and geochemistry of Zhushan metagabbro in Yilan, eastern Heilongjiang and its tectonic implication. *Glob. Geol.* 36, 413–427. doi:10.3969/j.issn.1004-5589

Zhu, Y., Zhao, G., Sun, M., Eizenhöfer, P. R., Liu, Q., and Liu, D. X. (2017c). Subduction between the Jiamusi and Songliao blocks: geochronological and geochemical constraints from granitoids within the Zhangguangcailing orogen, northeastern China. *Lithosphere* 9, 515–533. doi:10.1130/L618.1

Zhao, L., Guo, F., Fan, W., and Huang, M. (2018). Roles of Subducted Pelagic and Terrigenous Sediments in Early Jurassic Mafic Magmatism in NE China: Constraints on the Architecture of Paleo-Pacific Subduction Zone. *JGR Solid Earth* 124 (3), 2525–2550. doi:10.1029/2018JB016487